Delft University of Technology

**Document Version**
Final published version

**Licence**
CC BY

**Citation (APA)**
Agarwal, S., Gómez, S. S., & Colomés, O. (2026). Nonlinear dynamic response of mooring cables based on finite-strain theory: Finite element and reduced-order models. *Ocean Engineering*, *365*(P3), Article 127337. https://doi.org/10.1016/j.oceaneng.2026.127337

**Important note**
To cite this publication, please use the final published version (if applicable).
Please check the document version above.

**Copyright**
In case the licence states "Dutch Copyright Act (Article 25fa)", this publication was made available Green Open Access via the TU Delft Institutional Repository pursuant to Dutch Copyright Act (Article 25fa, the Taverne amendment). This provision does not affect copyright ownership.
Unless copyright is transferred by contract or statute, it remains with the copyright holder.

**Sharing and reuse**
Other than for strictly personal use, it is not permitted to download, forward or distribute the text or part of it, without the consent of the author(s) and/or copyright holder(s), unless the work is under an open content license such as Creative Commons.

**Takedown policy**
Please contact us and provide details if you believe this document breaches copyrights.
We will remove access to the work immediately and investigate your claim.

*This work is downloaded from Delft University of Technology.*

Ocean Engineering 365 (2026) 127337

Contents lists available at ScienceDirect

Ocean Engineering

journal homepage: www.elsevier.com/locate/oceaneng

Research paper

# Nonlinear dynamic response of mooring cables based on finite-strain theory: Finite element and reduced-order models ☆

Shagun Agarwal [a], Sergio Sánchez Gómez [a,b], Oriol Colomés [a,*]

[a] Delft University of Technology, Stevinweg 1, Delft, 2628 CN, The Netherlands
[b] Universitat Rovira i Virgili, Av. Països Catalans 26, Tarragona, 43007, Spain

ARTICLE INFO

*Keywords:*
Mooring dynamics
Finite strain theory
FEM
TDC
Catenary mooring
Taut mooring

ABSTRACT

This manuscript presents a formulation for mooring line dynamics using Tangential Differential Calculus (TDC) framework to handle geometric non-linearities in catenary and taut systems. Based on finite-strain theory, the model accounts for large deformations, self-weight, buoyancy, seabed interaction, and hydrodynamic drag. The study presents two solution procedures, GNL-FEM, a high-fidelity finite element model implemented in Julia, and GNL-ANA, a reduced-order semi-analytical model for efficient preliminary analysis.

For GNL-FEM, mesh and element order convergence studies demonstrate optimal performance, followed by validation against MoorDyn for catenary lines. In cases involving swell waves, GNL-FEM is shown to minimise the spurious oscillations typically observed in lumped-mass models during slack-line events. A primary focus of this manuscript is the dynamic behaviour of taut mooring lines under harmonic transverse excitation. GNL-FEM results demonstrate progressive geometric hardening, as the system's natural frequency increases with higher excitation amplitude. Furthermore, strain spectra exhibit distinct super-harmonics and sub-harmonics. GNL-ANA is shown to be accurate up to the second natural frequency, even under high pre-tension and excitation, providing a valuable tool for identifying energy hotspots and optimising material properties in synthetic lines. Overall, the framework provides a consistent and versatile basis for modelling complexities in mooring systems.

## 1. Introduction

As offshore renewable energy, e.g. offshore wind, wave or photovoltaic energy technologies, continues to grow (Soares-Ramos et al., 2020; Guo and Ringwood, 2021; Li et al., 2022; Bilgili and Alphan, 2022), water depth becomes one of the main challenges for their deployment at scale. Floating technologies can overcome this critical challenge, as demonstrated in several feasibility studies worldwide, see for example Bhuiyan et al. (2022), Castro-Santos et al. (2016) and Maienza et al. (2022).

With this expansion into floating structures, mooring systems become essential components for the viability of such technologies, as they are required for maintaining stability under variable ocean conditions, see Campanile et al. (2018), Xu et al. (2021), Harris et al. (2004), Kanotra and Shankar (2022) and references therein. It should be noted that for floating systems, the dynamic and non-linear behaviour of mooring lines is crucial for assessing the loads not only in extreme conditions, but also for peak loads during operating conditions (Harnois et al., 2016). Test campaigns such as DeepCWind have further emphasised the importance of dynamic analysis of mooring lines, demonstrating that the quasi-static approach systematically underestimates line tension and fails to account for key phenomena such as hydrodynamic drag, internal damping, line–line interactions, and dynamic contact with the seabed (Wendt et al., 2016).

For conventional systems, the dynamic effects are especially relevant during slack-line events (Hennessey et al., 2005; Qiao et al., 2020) and at the touch-down point while interacting with the sea-bed (Mavrakos et al., 1996; Chatjigeorgiou and Mavrakos, 2016). However, the new generation of floating renewable energy systems introduces additional challenges. The substructures of most offshore renewable platforms are relatively lightweight, both to reduce costs and because the superstructures they support do not require heavy foundations. Moreover, while these platforms are increasingly being deployed in deeper waters compared to early installations, the overall depths are still relatively shallow, typically within 200 m (Li et al., 2022; Campanile et al., 2018). Furthermore, the bathymetry across the farm scale can vary significantly, thus requiring a mooring system design for variable bathymetry (Mahfouz et al., 2024). These trends render traditional chain-based mooring systems less suitable, as such systems

☆ This article is part of a Special issue entitled: 'OE_Mooring and cable system' published in Ocean Engineering.

* Corresponding author.
*E-mail addresses:* s.agarwal@tudelft.nl (S. Agarwal), s.sanchezgomez-1@tudelft.nl (S.S. Gómez), j.o.colomesgene@tudelft.nl (O. Colomés).

https://doi.org/10.1016/j.oceaneng.2026.127337
Received 23 April 2026; Received in revised form 24 July 2026; Accepted 28 July 2026
Available online 6 August 2026
0029-8018/© 2026 The Authors. Published by Elsevier Ltd. This is an open access article under the CC BY license (http://creativecommons.org/licenses/by/4.0/).

are heavy, and, in shallower depths these may result in excessively long segments of line lying on the seabed. Consequently, there has been a growing shift towards using lightweight synthetic mooring lines for these applications. Unlike chain-based systems that rely primarily on the weight of the chain for their restoring force, synthetic lines depend on their material elasticity for providing the restoring force. However, the challenge is that the synthetic lines have non-linear and dynamic viscoelastic properties, i.e., their stiffness depends on the instantaneous load and loading history, Weller et al. (2015).

For offshore renewable farms, the use of mooring systems with shared mooring lines is an emerging trend. In shared mooring systems, multiple floating units are interconnected without each unit being directly anchored to the seabed. These configurations are gaining attention as cost-effective and environmentally friendly alternatives (Xie et al., 2024; Lozon and Hall, 2023; Zhang and Liu, 2023). However, they introduce an additional layer of complexity due to the dynamic interactions between the interconnected mooring lines and the floaters (Pham et al., 2021).

Another emerging trend in station-keeping of offshore renewables is the increasing use of taut mooring lines in intermediate water depths. Taut mooring systems offer several advantages, including a reduced seabed footprint, shorter and more cost-effective lines, higher stiffness, and improved load distribution (Bach-Gansmo et al., 2020). However, two key challenges in their implementation are anchor design and ensuring appropriate line stiffness. A critical nonlinear phenomenon often overlooked in the design of taut mooring systems is the variation in effective stiffness with excitation frequency and amplitude, primarily due to geometric nonlinearity. As highlighted in Niosi et al. (2025), there remains a significant gap in both experimental and numerical studies of taut mooring systems in the context of offshore renewables, particularly regarding the investigation of non-linear dynamic effects such as stiffness hardening under periodic excitation.

Therefore, alongside the growing demand for floating structures, there is an increasing need for accurate and efficient predictive tools capable of capturing the dynamic and non-linear behaviour of mooring lines under time-varying loads. This is especially critical in applications involving monitoring (Chen et al., 2023), control, and hybrid model testing (Vilsen et al., 2019), where simulations must often be performed in (or close to) real-time (Qiao et al., 2021; Cao et al., 2024).

In this context, the use of numerical or computational tools is preferred due to their capability of solving non-linear and dynamic problems. It is evident that in contemporary practice, the lumped-mass approach is the most widely adopted, primarily due to its computational efficiency (Masciola et al., 2014). Beginning with the early contributions of Walton and Polachek (1959), the lumped mass approach has been widely adopted in commercial software such as Orcaflex (Orcina, 2014) and Ansys Aqwa (Inc, 2024) to study the influence of mooring dynamics on floater response (Niosi et al., 2023; Zhao et al., 2023; Qin et al., 2025). ProteusDS (Ocean, 2018) employs a lumped-mass cable formulation, using a cubic-spline representation between nodes to additionally resolve bending and torsional stiffness (Buckham et al., 2004), and has been applied and evaluated for mooring load analysis of tidal current converters with taut mooring configurations (Jeffcoate et al., 2016; Bivol et al., 2017). Open-source tools like MoorDyn (Hall and Goupee, 2015), developed by NREL, have also been extensively used in conjunction with OpenFAST (Hall, 2020), as well as with high-fidelity time-domain solvers such as OpenFOAM (Aliyar et al., 2022; Yu et al., 2023) and DualSPHysics (Domínguez et al., 2019). As a result, this approach has become well-established and has played a key role in advancing mooring analysis from quasi-static models to fully dynamic simulations. The versatility of the lumped mass approach has been demonstrated across a range of applications, including the dynamic response of ships, offshore renewable systems such as wave energy converters and offshore wind farms, aquaculture installations, and oil and gas platforms.

The treatment of geometric nonlinearity in mooring lines has also been pursued through other approaches. A reduced order model of a cable was developed in Escalante et al. (2011) by applying proper orthogonal decomposition to the cubic spline finite element formulation of Buckham et al. (2004), which resolves both bending and torsional stiffness. Snap loads, which may be induced by sea-bed contact, or cable slack conditions (Vassalos and Kourouklis, 1998), are a particularly demanding test of these geometric nonlinearity treatments, since a lumped mass model resolves only a constant strain value per segment and tends to smear the resulting stress wave. To address this, a local discontinuous Galerkin finite element formulation was developed in Palm et al. (2017), which retains only extensional stiffness, but uses an hp-adaptive scheme and a Riemann solver to resolve the stress wave propagation associated with snap loads. A finite difference formulation in a Frenet frame was developed in Chen et al. (2018), includes bending and torsional stiffness in addition to the axial one (Chen et al., 2018). More recently, a torsion and shear-free Kirchhoff rod formulation for mooring lines was proposed by Roccia et al. (2025), with a penalty-based barrier function for the seabed contact, and verified against the elastic catenary solution and against OpenFAST. Several of these formulations were directly compared in Zhong et al. (2024) to assess their suitability for floating offshore wind turbine (FOWT) analysis. The local discontinuous Galerkin finite element and lumped mass formulations were found to be best suited for coupled FOWT analysis, while the accuracy of the lumped mass and finite difference formulations was shown to be lower for high frequency excitation and snap-load conditions. While these studies demonstrate that geometric nonlinearity arising from large displacement and rotation has been considered extensively in the mooring literature, the treatment of geometric nonlinearity arising from the finite-strain kinematics of the cable, i.e., the nonlinear coupling between strain and displacement gradients, remains comparatively unaddressed.

We briefly touch upon the treatment of material nonlinearity in mooring lines. Existing lumped-mass formulations are typically developed under the assumption that the contribution of strain acceleration is negligible (Buckham et al., 2004). While this assumption has proven effective for linear elastic materials, it may not be valid for viscoelastic materials, where the time-dependent nature of the response could render strain acceleration significant (Haj-Ali and Muliana, 2004; Banks et al., 2011). A few approaches have since addressed material nonlinearity in mooring lines directly. This can be as simple as an empirical, load-history dependent stiffness expression (Depalo et al., 2022), where a dynamic axial stiffness model for synthetic fibre ropes is shown to predict mooring tensions 30%–40% higher than those obtained from a quasi-static nonlinear stiffness curve. Within the lumped mass framework, Li and Choung (2021) extended the formulation to include strain and strain-rate dependent stiffness, and found that this nonlinear stiffness has a measurable effect on the motion of taut-leg, but not catenary, floating platforms. Nguyen and Thiagarajan (2022) instead proposed a numerical inversion scheme to recover a Schapery nonlinear viscoelastic constitutive model from strain-based experimental data, and incorporated it within the MoorDyn lumped mass model. They assess line tensions under gusts and snap loads, finding that neglecting the time-dependent effects can overestimate mean mooring loads by up to 16%. There has been little development on incorporating material nonlinearity within the discontinuous Galerkin finite element or Kirchhoff rod formulations discussed earlier. Hence, a formulation that captures both the geometric nonlinearity of the cable and the dynamic, history-dependent stiffness of synthetic materials, within a single continuous and displacement-based framework, is still missing from the literature.

The aim of this paper therefore is to define a mooring dynamics model which can be applied to a variety of mooring systems, including catenary lines of conventional floating systems and taut lines of tension leg platforms or spar platforms. The model should be conducive to the geometric nonlinearity arising from the shape of the line and finite-strain kinematics of the line. Additionally, the model should be capable of accommodating the dynamic non-linear stiffness of viscoelastic materials employed in synthetic mooring lines. With these goals in mind, the primary contribution of this manuscript is the formulation of the boundary value problem of mooring line dynamics using Tangential Differential Calculus (TDC).

A TDC-based formulation offers several advantages. First, it is inherently defines the partial differential equations along curved manifolds, which simplifies the definition of the physical problem and associated boundary conditions. Second, it provides numerical versatility, allowing the problem to be solved using various approaches, including parametrisation and embedded methods. Third, it enables the definition of differential and geometric quantities at a continuous level using tangents, in contrast to the piecewise definitions found in many conventional computational techniques. This can be especially convenient for defining the viscoelastic terms for synthetic mooring systems. The versatility of the TDC has been shown for ropes and membranes in Fries and Schöllhammer (2020), linear Kirchhoff beams on curved manifolds in Kaiser and Fries (2023) and shells, plates and beams in Sky et al. (2024). Therefore this approach is ideal not only for the axial response of the mooring lines, but also for bending and torsional effects.

Building on this TDC-based formulation, the manuscript is structured around three contributions. First, we develop a finite-element solution procedure, GNL-FEM, based on finite-strain theory, accounting for self-weight, buoyancy, seabed interaction, and hydrodynamic drag, applicable to both catenary and taut mooring lines. The robustness of GNL-FEM is established through mesh size ($h$) and element order ($p$) convergence studies, and its accuracy is validated against MoorDyn for catenary lines and against an established benchmark for the static finite-strain problem. Second, we use GNL-FEM to investigate the nonlinear dynamic response of taut mooring lines under harmonic transverse excitation. We examine how increasing pre-tension, excitation frequency, and amplitude drive geometric hardening behaviour and the resulting super- and sub-harmonics in the strain response. Third, we develop a reduced-order semi-analytical alternative, GNL-ANA, for the taut mooring line, and investigate its scope of validity. This provides a useful tool for low-fidelity analyses, such as property optimisation and conceptual design.

Since the focus of this manuscript is the development of the mooring analysis model, the manuscript presents results with a single mooring line exposed to periodic excitation. The present manuscript focuses specifically on demonstrating the geometric nonlinearity arising from the finite-strain kinematics of the mooring line, and the material properties considered are restricted to a linear elastic model. Material nonlinearity is discussed only as motivation for the formulation's design and is not demonstrated in the present results. It is instead addressed in our work (Agarwal and Colomés, 2025).

The manuscript is organised as follows. Section 2 defines the geometric and structural problem, including the equilibrium and external forcing. Section 3 presents the solution procedures, with Section 3.1 focusing on the finite-element model and Section 3.2 presenting the reduced-order analytical model. Section 4 presents validation and case studies, examining the convergence and accuracy of GNL-FEM, the dynamic response of taut and catenary lines, and the range of applicability of GNL-ANA.

## 2. Problem setting

### 2.1. Definition of the geometric problem

The numerical formulation is developed for a flexible rope with large displacements. For these structures, it is essential to distinguish between the un-deformed and deformed configurations. In such cases, physical equilibrium is satisfied in the deformed configuration. Such analysis is often referred to as geometrically nonlinear analysis, or finite-strain analysis. We utilise the approach of Tangential Differential Calculus (TDC) (Fries and Schöllhammer, 2020) to compute the differential and geometric quantities required for evaluating the field variables along the deforming cable. This framework allows for a consistent and robust formulation of the kinematics and mechanics on curved geometries such as mooring lines undergoing large deformations.

We denote the un-deformed and deformed configurations as $\Gamma_{\boldsymbol{X}}$ (un-deformed) and $\Gamma_{\boldsymbol{x}}$ (deformed), respectively, following the convention of upper case letter for undeformed configuration and lowercase letters for deformed configuration, consistent with Fries and Schöllhammer (2020). In this manuscript we restrict our analysis to a 2D problem. Therefore, $\Gamma_{\boldsymbol{X}}$ and $\Gamma_{\boldsymbol{x}}$ are 1-dimensional manifolds, immersed in 2-dimensional space, $\mathbb{R}^2$. The difference between the two configurations is the displacement field $\boldsymbol{u}(\boldsymbol{X})$, i.e

$$\boldsymbol{x}(\boldsymbol{X},t) = \boldsymbol{X} + \boldsymbol{u}(\boldsymbol{X},t) \quad \text{where } \boldsymbol{X} \in \Gamma_{\boldsymbol{X}} \subset \mathbb{R}^2 \text{ and } \boldsymbol{x} \in \Gamma_{\boldsymbol{x}} \subset \mathbb{R}^2 \tag{1}$$

The definition of strain on $\Gamma_{\boldsymbol{X}}$ and $\Gamma_{\boldsymbol{x}}$ first requires definition of certain geometric and differential quantities. We briefly present the necessary quantities for parameterised formulation of 1D manifolds in 2D space in this section. We refer the readers to Fries and Schöllhammer (2020) for the derivation of these quantities for cables and membranes in 2D and 3D domains.

For cables and ropes, the $\Gamma_{\boldsymbol{X}}$ and $\Gamma_{\boldsymbol{x}}$ manifolds can be parameterised using a 1-dimensional reference domain, $\Omega_r \subset \mathbb{R}^1$. Hence, there exists a map $\boldsymbol{X}(\boldsymbol{r}) : \mathbb{R}^1 \to \mathbb{R}^2$ from 1-dimensional reference domain to 2 dimensional space, as indicated in Fig. 1. We define the components as $\boldsymbol{X} = [X, Z]^T$ and $\boldsymbol{r} = [r]^T$. Subsequently the Jacobian matrix is given by the following $(2 \times 1)$ matrix.

$$\mathbf{J}(\boldsymbol{r}) = \frac{\partial \boldsymbol{X}(\boldsymbol{r})}{\partial \boldsymbol{r}} = \nabla_r \boldsymbol{X}(\boldsymbol{r}) = \begin{bmatrix} \frac{\partial X}{\partial r} & \frac{\partial Z}{\partial r} \end{bmatrix}^T \tag{2}$$

Here, the Jacobi also represents the tangent to the manifold $\Gamma_{\boldsymbol{X}}$ at point $\boldsymbol{X}$. In the 2D scenario, the manifold $\Gamma_{\boldsymbol{X}}$ will only have a single tangent, denoted as $\boldsymbol{T}^* = \mathbf{J}(\boldsymbol{r})$, with the unit tangent vector given by $\boldsymbol{T} = \frac{\boldsymbol{T}^*}{\|\boldsymbol{T}^*\|}$. The Jacobi matrix is further used to compute the following geometric quantities, which are required for calculating the *surface gradient*.

$$\mathbf{G} = \mathbf{J}^T \cdot \mathbf{J} \quad (1 \times 1) \text{ matrix} \qquad \mathbf{Q} = \mathbf{J} \cdot \mathbf{G}^{-1} \quad (2 \times 1) \text{ matrix} \tag{3}$$

The displacement vector field, denoted as $\boldsymbol{u} = [u, w]^T$, is parameterised using the same reference domain $\Omega_r$. However, this displacement field is only defined on the surface $\Gamma_{\boldsymbol{X}}$. As a result, the standard gradient of $\boldsymbol{u}$ with respect to the 2D space cannot be applied. Instead, the gradient of $\boldsymbol{u}$ is defined along the manifold $\Gamma_{\boldsymbol{X}}$, which is referred to as the *directional surface gradient*. For the vector field $\boldsymbol{u}$, the surface gradient is given by

$$\nabla_{\boldsymbol{X}}^{\Gamma,\text{dir}} \boldsymbol{u}(\boldsymbol{r}) = \begin{bmatrix} (\nabla_{\boldsymbol{X}}^{\Gamma} u)^T \\ (\nabla_{\boldsymbol{X}}^{\Gamma} w)^T \end{bmatrix} = \begin{bmatrix} \nabla_X^{\Gamma} u & \nabla_Z^{\Gamma} u \\ \nabla_X^{\Gamma} w & \nabla_Z^{\Gamma} w \end{bmatrix} = \nabla_{\boldsymbol{r}} \boldsymbol{u}(\boldsymbol{r}) \cdot \mathbf{Q}^T \tag{4}$$

We next define these geometric and differential quantities on the deformed manifold $\Gamma_{\boldsymbol{x}}$. By utilising the map from $\Gamma_{\boldsymbol{X}}$ to $\Gamma_{\boldsymbol{x}}$ defined in Eq. (1), we define a Jacobian called the *surface deformation gradient* $\mathbf{F}_\Gamma$, given by

$$\mathbf{F}_\Gamma = \nabla_{\boldsymbol{X}}^{\Gamma,\text{dir}} \boldsymbol{x}(\boldsymbol{X}) = \mathbf{I} + \nabla_{\boldsymbol{X}}^{\Gamma,\text{dir}} \boldsymbol{u}(\boldsymbol{X}) \tag{5}$$

Here $\mathbf{I}$ is a $(2\times 2)$ identity matrix. The surface deformation gradient $\mathbf{F}_\Gamma$ is a geometric quantity that maps tangent vectors from the undeformed configuration $\Gamma_{\boldsymbol{X}}$ to the deformed configuration $\Gamma_{\boldsymbol{x}}$. Using $\mathbf{F}_\Gamma$, we can calculate the Jacobi matrix and the corresponding tangent and unit tangent to $\Gamma_{\boldsymbol{x}}$ as $\mathbf{j} = \mathbf{F}_\Gamma \cdot \mathbf{J}$, $\boldsymbol{t}^* = \mathbf{F}_\Gamma \cdot \boldsymbol{T}^*$ and $\boldsymbol{t} = \frac{\boldsymbol{t}^*}{\|\boldsymbol{t}^*\|}$.

The final set of geometric quantities are the projectors $\mathbf{P}$ and $\mathbf{p}$ for $\Gamma_{\boldsymbol{X}}$ and $\Gamma_{\boldsymbol{x}}$, respectively, the curvature unit normal $\boldsymbol{N}$ and $\boldsymbol{n}$ for $\Gamma_{\boldsymbol{X}}$ and $\Gamma_{\boldsymbol{x}}$, respectively, and the stretch $\Lambda$ of a differential element, given as follows.

$$\mathbf{P} = \boldsymbol{T} \otimes \boldsymbol{T} \tag{6}$$

$$\mathbf{p} = \boldsymbol{t} \otimes \boldsymbol{t} \tag{7}$$

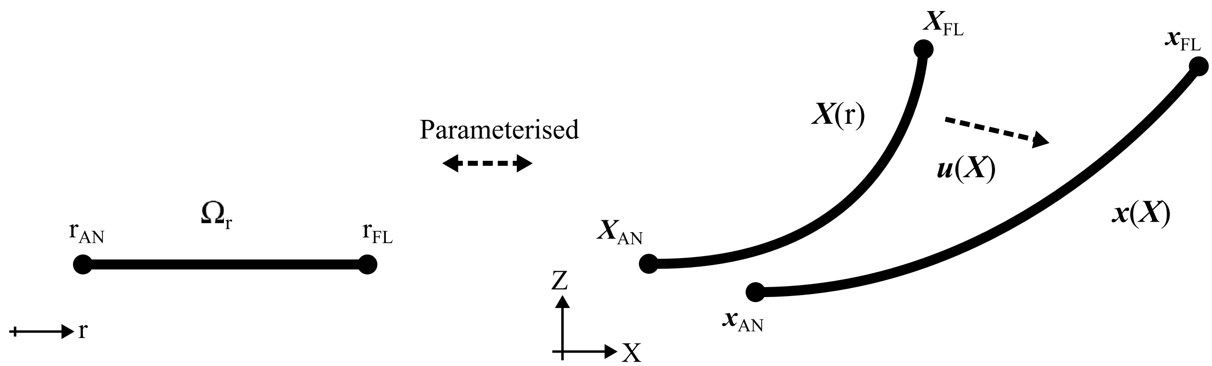


**Fig. 1.** A schematic of a 1-dimensional reference domain $\Omega_r$ for the cable, which is mapped to an un-deformed configuration $\Gamma_X$ via the map $X(r)$, and a dynamic deformed configuration $\Gamma_x$ using the map $x(r)$.

$$\boldsymbol{N} = \begin{bmatrix} 0 & -1 \\ 1 & 0 \end{bmatrix} \cdot \boldsymbol{T} \tag{8}$$

$$\boldsymbol{n} = \begin{bmatrix} 0 & -1 \\ 1 & 0 \end{bmatrix} \cdot \boldsymbol{t} \tag{9}$$

$$\Lambda = \frac{\|\boldsymbol{t}^*\|}{\|\boldsymbol{T}^*\|} \tag{10}$$

### 2.2. Definition of the structural problem

With the geometric quantities defined, we can now express the finite-strain theory strain and stress tensor for the cable. The strain tensors on the un-deformed $\Gamma_X$ are given by the directional and tangential Cauchy–Green tensor as follows

$$\mathbf{E}_{\text{dir}} = \frac{1}{2} \cdot \left(\mathbf{F}_\Gamma^T \cdot \mathbf{F}_\Gamma - \mathbf{I}\right) \tag{11}$$

$$\mathbf{E}_{\text{tang}} = \mathbf{P} \cdot \mathbf{E}_{\text{dir}} \cdot \mathbf{P} \tag{12}$$

Similarly, the directional and tangential Euler–Almansi strain tensors on $\Gamma_x$ are given by,

$$\mathbf{e}_{\text{dir}} = \frac{1}{2} \cdot \left(\mathbf{I} - (\mathbf{F}_\Gamma \cdot \mathbf{F}_\Gamma^T)^{-1}\right) \tag{13}$$

$$\mathbf{e}_{\text{tang}} = \mathbf{p} \cdot \mathbf{e}_{\text{dir}} \cdot \mathbf{p} \tag{14}$$

In this manuscript we restrict the analysis to Saint Venant–Kirchhoff solids. For cables made of material with Young's modulus $E$ and Poisson's ratio $\nu$, the corresponding Lamé constants are $\lambda = 0$ and $\mu = \frac{E}{2(1+\nu)}$. Consequently, the first and second Piola–Kirchhoff stress tensors $\mathbf{K}$, $\mathbf{S}$ on $\Gamma_X$ and the Cauchy stress tensor $\sigma$ on $\Gamma_x$ are expressed as follows,

$$\mathbf{S} = 2\mu \cdot \mathbf{E}_{\text{tang}} \tag{15}$$

$$\mathbf{K} = \mathbf{F}_\Gamma \cdot \mathbf{S} \tag{16}$$

$$\sigma = \frac{1}{\Lambda} \cdot \mathbf{F}_\Gamma \cdot \mathbf{S} \cdot \mathbf{F}_\Gamma \tag{17}$$

### 2.3. Equilibrium

The equilibrium of the problem is defined in the deformed configuration $\Gamma_x$. For the cable, the equilibrium per unit volume is defined as

$$\rho\, \ddot{\boldsymbol{u}} - \text{div}_\Gamma\, \sigma(\boldsymbol{u}) - \boldsymbol{b}(\boldsymbol{x}) = 0 \quad \forall \boldsymbol{x} \in \Gamma_{\boldsymbol{x}} \tag{18}$$

where, $\rho$ is the density, $\boldsymbol{b}(\boldsymbol{x})$ are the external body forces on the cable in the deformed configuration.

Fig. 2 shows a schematic of the mooring line problem, highlighting the external forces acting on the line, including the action due to gravity, buoyancy, parameterised wave drag, current drag, and interactions with the sea-bed. As these forces vary along the length of the line, they are described per unit length. The self-weight of the line is expressed as

$$\boldsymbol{b}_{\text{weight}}(\boldsymbol{x}) = -\rho\, A\, g\, \hat{k}, \tag{19}$$

where $g$ is the gravitational acceleration and $\hat{k}$ is the vertical unit vector. The buoyancy force corresponds to the weight of the displaced water and is given by

$$\boldsymbol{b}_{\text{buoyancy}}(\boldsymbol{x}) = \rho_{\text{water}}\, A_{\text{disp}}\, g\, \hat{k}, \tag{20}$$

where $\rho_{\text{water}}$ is the density of water and $A_{\text{disp}}$ represents the displaced volume per unit length. The sea-bed interaction is modelled via a damped spring force that is activated only when the line comes into contact with the sea-bed:

$$\boldsymbol{b}_{\text{bed}}(\boldsymbol{x}) = \begin{cases} -k_b \left(z - z_{\text{bed}}\right) \hat{k} - c_b \dot{z}\, \hat{k} & \text{if } z \le z_{\text{bed}}, \\ 0 & \text{if } z > z_{\text{bed}}. \end{cases} \tag{21}$$

Numerically, the sea-bed contact is enabled using a Heaviside step function.

The drag force on the line comprises contributions from (1) self-drag, (2) action of currents, and (3) wave action. If $\boldsymbol{v}_{\text{wave}}(\boldsymbol{x})$ and $\boldsymbol{v}_{\text{current}}(\boldsymbol{x})$ denote the local wave and current velocities, respectively, the drag force is computed as:

$$\boldsymbol{b}_{\text{drag},n}(\boldsymbol{x}) = \frac{1}{2} \rho_{\text{water}}\, C_{d,n}\, \boldsymbol{v}_{r,n}(\boldsymbol{x}) \left|\boldsymbol{v}_{r,n}(\boldsymbol{x})\right|, \tag{22}$$

$$\boldsymbol{b}_{\text{drag},t}(\boldsymbol{x}) = \frac{1}{2} \rho_{\text{water}}\, C_{d,t}\, \boldsymbol{v}_{r,t}(\boldsymbol{x}) \left|\boldsymbol{v}_{r,t}(\boldsymbol{x})\right|, \tag{23}$$

$$\text{where} \quad \boldsymbol{v}_r(\boldsymbol{x}) = \boldsymbol{v}_{\text{wave}}(\boldsymbol{x}) + \boldsymbol{v}_{\text{current}}(\boldsymbol{x}) - \dot{\boldsymbol{u}}(\boldsymbol{x}), \tag{24}$$

$$\boldsymbol{v}_{r,t}(\boldsymbol{x}) = \left(\boldsymbol{v}_r(\boldsymbol{x}) \cdot \hat{\imath}(\boldsymbol{x})\right) \hat{\imath}(\boldsymbol{x}), \tag{25}$$

$$\boldsymbol{v}_{r,n}(\boldsymbol{x}) = \boldsymbol{v}_r(\boldsymbol{x}) - \boldsymbol{v}_{r,t}(\boldsymbol{x}). \tag{26}$$

In the current analysis, the influence of added mass and added damping of the mooring line is neglected, consistent with the findings of Hall and Goupee (2015), which suggest that their effect on the overall system response is minimal. The equivalent strong form of the equilibrium transformed to the un-deformed configuration $\Gamma_X$, per unit volume is defined as

$$\rho_0\, \ddot{\boldsymbol{u}}(\boldsymbol{X}) - \text{Div}_\Gamma\, \mathbf{K}(\boldsymbol{u}) - \boldsymbol{B}(\boldsymbol{X}) = 0 \quad \forall \boldsymbol{X} \in \Gamma_{\boldsymbol{X}}, \tag{27}$$

$$\text{where,} \quad \text{Div}_\Gamma\, \mathbf{K}(\boldsymbol{u}) = \begin{bmatrix} \nabla_r K_{11} & \nabla_r K_{12} \\ \nabla_r K_{21} & \nabla_r K_{22} \end{bmatrix} \cdot \mathbf{Q}. \tag{28}$$

where, $\rho_0$ is the density, $\text{Div}_\Gamma\, \mathbf{K} = \nabla_{\boldsymbol{X}}^{\Gamma,\text{dir}} \cdot \mathbf{K}$ is the divergence of the first Piola–Kirchhoff stress tensor, $\boldsymbol{B}(\boldsymbol{X}) = [B_1, B_2]^T$ are the external body forces on the cable in the un-deformed configuration. We can now utilise the strong form Eq. (27) for defining the analytical and numerical solution to the dynamics of a flexible cable.

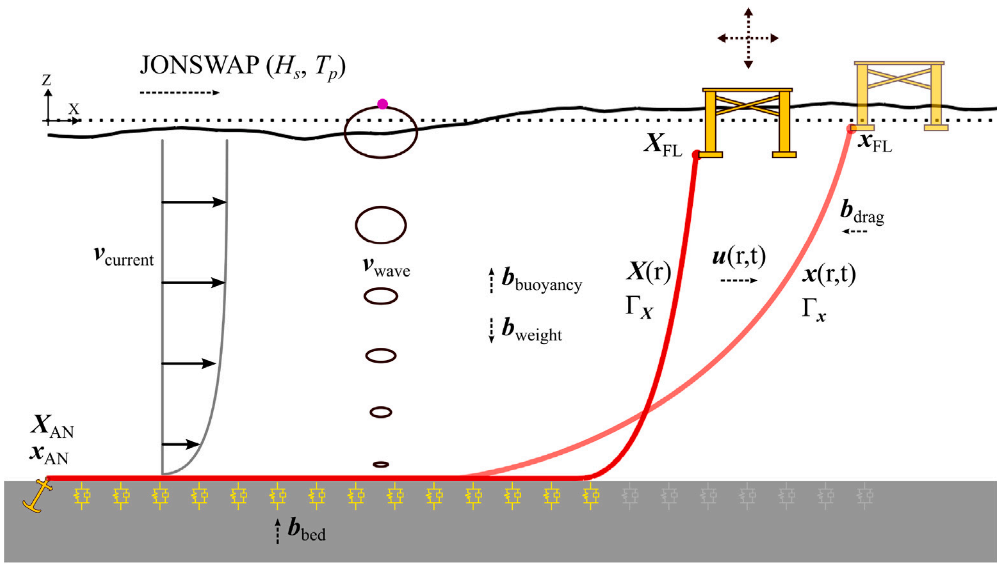


**Fig. 2.** Schematic of the catenary mooring line problem, with the external body forces and spring-dashpot implementation of the sea-bed.

### 2.4. Boundary conditions

The cable boundaries of the cable are denoted as $\partial\Gamma_X$ for the undeformed configuration $\Gamma_X$ and $\partial\Gamma_x$ for the deformed configuration $\Gamma_x$. The boundary condition can be prescribed either by specifying the displacement field on Dirichlet boundaries $\partial\Gamma_{X,D}$, or through the forces at Neumann boundaries $\partial\Gamma_{X,N}$.

$$\boldsymbol{u}(\boldsymbol{X}) = \hat{\boldsymbol{u}}(\boldsymbol{X}) \quad \text{on } \partial\Gamma_{X,D} \tag{29}$$

$$\mathbf{K}(\boldsymbol{X}) \cdot \mathbf{N}_{\partial\Gamma_X} = \mathbf{H}(\boldsymbol{X}) \quad \text{on } \partial\Gamma_{X,N} \tag{30}$$

### 2.5. Energy quantities and Lagrangian formalism

The mechanical energy density in an elastic cable as the one given in the problem at hand can be formulated as follows,

$$e_{\mathrm{m}} = k_{\mathrm{kinetic}} + u_{\mathrm{strain}} = \frac{1}{2}\,\rho\,|\boldsymbol{u}|^2 + \frac{1}{2}\,\mathbf{e}_{\mathrm{tang}} : \boldsymbol{\sigma} \tag{31}$$

where the kinetic $k_{\mathrm{kinetic}}$ and potential $u_{\mathrm{strain}}$ energy densities are defined in Eq. (31). By using the procedure described in Appendix, the equation of motion of a 1-dimensional continuous system is formulated,

$$\frac{\partial\lambda}{\partial u_i} + \frac{\partial}{\partial t}\frac{\partial\lambda}{\partial\dot{u}_i} + \frac{\partial}{\partial x_j}\frac{\partial\lambda}{\partial u_{i,j}} + \frac{\partial\mathscr{D}_{\mathrm{diss}}}{\partial\dot{u}_i} = 0 \tag{32}$$

where $u_i$ are the components of the displacement field $\boldsymbol{u}(\boldsymbol{X},t)$, and $\lambda$ is the Lagrangian function defined as,

$$\lambda = \int_A \left(k_{\mathrm{kinetic}} - u_{\mathrm{strain}}\right) dA \tag{33}$$

By substituting Eqs. (31) to (33) and (32), the equations of motion described in Eq. (39) for the displacements in the longitudinal $w(X,t)$ and transverse $u(X,t)$ directions are formulated, with the boundary conditions described by Eq. (34).

### 2.6. Particular case: $\Gamma_X$ is a taut vertical line

The presented formulation defines the geometrically nonlinear problem for cables with arbitrary 2D conjurations. In this section, we present the problem for a taut vertical cable to illustrate the formulation for a simplified scenario.

Consider a line of length $L_0$ with the undeformed configuration denoted by $\boldsymbol{X} = [0, r]^T$, where the parameter $r \in [0, L_0]$. A schematic of this setup is shown in Fig. 3. The boundaries of this cable are identified as the anchor at $\boldsymbol{X}_{\mathrm{AN}} = \boldsymbol{X}(r=0) = [0,0]^T$ and the fairlead at $\boldsymbol{X}_{\mathrm{FL}} = \boldsymbol{X}(r=L_0) = [0, L_0]^T$. We initially pre-stretch the cable by applying axial elongation. Subsequently, we introduce harmonic excitation by moving the fairlead sinusoidally in the transverse direction. The corresponding boundary conditions at the anchor and fairlead are as follows,

$$\boldsymbol{u}_{\mathrm{AN}} = [0,0]^T \tag{34a}$$

$$\boldsymbol{u}_{\mathrm{FL}} = [a_p \sin(2\pi f_p t), \epsilon_0 L_0]^T \tag{34b}$$

where, $\epsilon_0$ is the initial axial stretch, while $a_p$ and $f_p$ are the amplitude and the frequency of the transverse excitation at the fairlead.

The geometric and differential quantities for this scenario are as follows.

$$\mathbf{J} = [0,1]^T, \quad \mathbf{Q} = [0,1]^T, \quad \boldsymbol{T} = [0,1]^T, \quad \mathbf{P} = \begin{bmatrix} 0 & 0 \\ 0 & 1 \end{bmatrix} \tag{35}$$

If the displacement field $\boldsymbol{u}(\boldsymbol{r}) = [\,u(r),\ w(r)\,]^T$, then the surface deformation gradient $\mathbf{F}_\Gamma$ is

$$\mathbf{F}_\Gamma = \begin{bmatrix} 1 & u' \\ 0 & 1+w' \end{bmatrix} \tag{36}$$

Then corresponding strain and stress tensors are given by

$$\mathbf{E}_{\mathrm{tang}} = \begin{bmatrix} 0 & 0 \\ 0 & w' + \frac{1}{2}\left(u'^2 + w'^2\right) \end{bmatrix} \tag{37}$$

$$\begin{aligned}\mathbf{K} &= \begin{bmatrix} 0 & \mu\, u'\left(u'^2 + (1+w')^2 - 1\right) \\ 0 & \mu\,(1+w')\left(u'^2 + (1+w')^2 - 1\right) \end{bmatrix} \\ &= \begin{bmatrix} 0 & \mu\left(u'^3 + u'w'^2 + 2u'w'\right) \\ 0 & \mu\left(w'^3 + u'^2 w' + u'^2 + 3w'^2 + 2w'\right) \end{bmatrix}\end{aligned} \tag{38}$$

The equilibrium from Eq. (27) is given by

$$\rho_0 \begin{bmatrix} \ddot{u} \\ \ddot{w} \end{bmatrix} - \mu \begin{bmatrix} u''w'\left(w'+2\right) + 2u'\left(w'+1\right)w'' + 3u'^2 u'' \\ u'^2 w'' + 2u'u''\left(1+w'\right) + \left(3w'^2 w'' + 6w'w'' + 2w''\right) \end{bmatrix} - \begin{bmatrix} B_1 \\ B_2 \end{bmatrix} = \begin{bmatrix} 0 \\ 0 \end{bmatrix} \tag{39}$$

We analyse this simplified scenario to explain the underlying physics using both numerical and analytical solution approaches. However, beyond serving as a conceptual tool, this scenario also has practical relevance. A vertical taut mooring line is analogous to the tendons of a tension leg platform (TLP), which is increasingly considered for

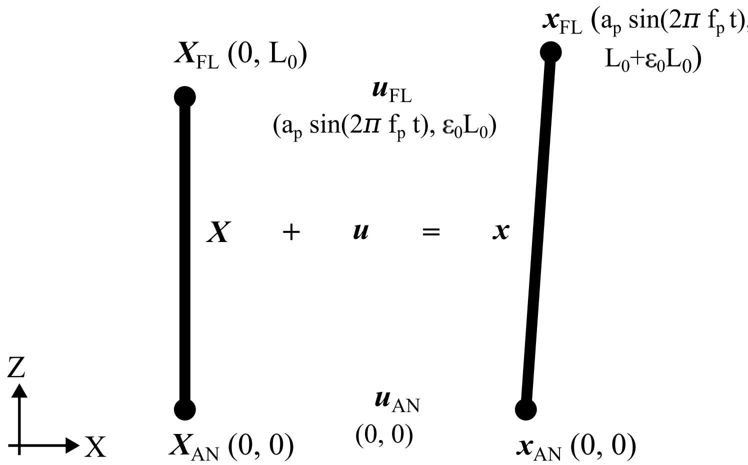


**Fig. 3.** Schematic of Scenario 1: $\Gamma_X$ is a vertical line.

deep-water wind turbines due to its lightweight substructure, minimal drift motion, smaller seabed footprint, and lower material costs. As TLPs are deployed in deeper waters, their linear natural frequency decreases, making them more susceptible to transverse excitation from cyclic wave loads, potentially leading to responses beyond the first mode. This study, therefore, provides valuable insights into both the solution methodology and the dynamic response characteristics of TLP tendons.

## 3. Solution procedure

### 3.1. Numerical model

We formulate a numerical problem for the defined problem definition using the finite-element method. In order to define the weak form, we establish the following functional spaces in the undeformed configuration $\Gamma_X$ and the reference domain $\Omega_r$.

$$\mathcal{V} = \left\{ \mathbf{v} \in H^1(\Gamma_{\boldsymbol{X}}) \right\} \tag{40}$$

$$\mathcal{V}_r = \left\{ \mathbf{v} \in H^1(\Omega_r) \right\} \tag{41}$$

With $H^1(\Omega)$ being the space of functions whose distributional first order derivatives have a bounded $L^2$-norm. The displacement field $\boldsymbol{u} \in \mathcal{V}$ and the corresponding test function $\boldsymbol{w} \in \mathcal{V}$. Therefore, the weak form of the equilibrium, defined on $\Gamma_X$ is given by

$$A \int_{\Gamma_X} \rho_0\, \boldsymbol{w} \cdot \ddot{\boldsymbol{u}}\, d\Gamma - A \int_{\Gamma_X} \boldsymbol{w} \cdot \mathrm{Div}_\Gamma\, \mathbf{K}(\boldsymbol{u})\, d\Gamma - A \int_{\Gamma_X} \boldsymbol{w} \cdot \boldsymbol{B}(\boldsymbol{X})\, d\Gamma = 0 \tag{42}$$

where $A$ is the cross-sectional area of the cable. The integration by parts of manifolds is given by (Delfour and Zolésio, 1996)

$$\int_{\Gamma_X} \boldsymbol{w} \cdot \mathrm{Div}_\Gamma\, \mathbf{K}(\boldsymbol{u})\, d\Gamma = - \int_{\Gamma_X} \nabla_{\boldsymbol{X}}^{\Gamma,\mathrm{dir}} \boldsymbol{w} : \mathbf{K}(\boldsymbol{u})\, d\Gamma + \int_{\partial \Gamma_X} \boldsymbol{w} \cdot \mathbf{K} \cdot \mathbf{N}_{\partial \Gamma_X}\, d\partial\Gamma + \int_{\Gamma_X} \chi\, \boldsymbol{w} \cdot \mathbf{K} \cdot \mathbf{N}\, d\Gamma \tag{43}$$

where, $\chi$ denotes the mean curvature. As highlighted in Fries and Schöllhammer (2020), for in plane tensors such as $\mathbf{K}$, the term involving $\chi$ vanishes. On substituting Eq. (43) in Eq. (42) and applying the Neumann boundary condition from Eq. (30), we get the final weak form

$$A \int_{\Gamma_X} \rho_0\, \boldsymbol{w} \cdot \ddot{\boldsymbol{u}}\, d\Gamma + A \int_{\Gamma_X} \nabla_{\boldsymbol{X}}^{\Gamma,\mathrm{dir}} \boldsymbol{w} : \mathbf{K}(\boldsymbol{u})\, d\Gamma - A \int_{\Gamma_X} \boldsymbol{w} \cdot \boldsymbol{B}\, d\Gamma - \int_{\partial\Gamma_X} \boldsymbol{w} \cdot \mathbf{H}\, d\partial\Gamma = 0 \tag{44}$$

The equivalent weak form in the reference configuration is written as

$$A \int_{\Omega_r} \rho_0\, \boldsymbol{w} \cdot \ddot{\boldsymbol{u}}\, \|\mathbf{J}\|\, d\Omega + A \int_{\Omega_r} \left( \nabla_{\boldsymbol{r}} \boldsymbol{w} \cdot \mathbf{Q}^T \right) : \mathbf{K}(\boldsymbol{u})\, \|\mathbf{J}\|\, d\Omega - A \int_{\Omega_r} \boldsymbol{w} \cdot \boldsymbol{B}\, \|\mathbf{J}\|\, d\Omega - \int_{\partial\Omega_r} \boldsymbol{w} \cdot \mathbf{H}\, d\partial\Omega = 0 \tag{45}$$

#### 3.1.1. Spatial and temporal discretisation

The discretised problem is formulated on a triangulation $\Omega_{r,h}$ of the reference domain $\Omega_r$. In order to get the discretised undeformed configuration, we map the discretised elements from the reference domain $\Omega_{r,h}$ via the mapping function $\boldsymbol{X}(\boldsymbol{r})$.

$$\mathcal{V}_{r,h} = \left\{ \mathbf{v_h} \in C^0(\Omega_r) : v_{h|K} \in (\mathbb{P}_s(K))^d, \forall K \in \Omega_{r,h} \right\} \tag{46}$$

$$\mathcal{V}_h = \left\{ \mathbf{v_h} = \boldsymbol{X}(\boldsymbol{r})_K, \forall K \in \Omega_{r,h} \right\} \tag{47}$$

Here $\mathbb{P}_s(K)$ is the space of Lagrange polynomials of degree $r$ for an element $K$ in $\Omega_{r,h}$. The discretised displacement $\boldsymbol{u}_h \in \mathcal{V}_h$ and test function $\boldsymbol{w}_h \in \mathcal{V}_h$, resulting in the following discretised weak form.

$$A \int_{\Omega_{r,h}} \rho_0\, \boldsymbol{w}_h \cdot \ddot{\boldsymbol{u}}_h\, \|\mathbf{J}\|\, d\Omega + A \int_{\Omega_{r,h}} \left( \nabla_{\boldsymbol{r}} \boldsymbol{w}_h \cdot \mathbf{Q}^T \right) : \mathbf{K}(\boldsymbol{u}_h)\, \|\mathbf{J}\|\, d\Omega - A \int_{\Omega_{r,h}} \boldsymbol{w}_h \cdot \boldsymbol{B}(\boldsymbol{X})\, \|\mathbf{J}\|\, d\Omega - \int_{\partial\Omega_r} \boldsymbol{w}_h \cdot \mathbf{H}(\boldsymbol{X})\, d\partial\Omega = 0 \tag{48}$$

The time discretisation of the second-order ODE is carried out using the Generalised-$\alpha$ method (Gobat and Grosenbaugh, 2001), with the asymptotic annihilation condition set as $\rho_\infty = 0$. This method enables the control of dissipation of high-frequency oscillations in the simulation. A constant time step $\Delta t$ is employed throughout the simulation. With this setup, the response with frequency higher than $f > 1/(10\Delta t)$ will be dissipated out of the simulation (Chung and Hulbert, 1993).

#### 3.1.2. Implementation in Gridap Julia

The implementation of this FE formulation is done in *Julia* programming language using a open-source finite-element library *Gridap.jl* (Badia and Verdugo, 2020). This library facilitates a simple yet powerful implementation of a finite-element problem, with the flexibility of choosing various continuous and discontinuous finite-element spaces, a convenient method of implementing the weak form similar to writing the equation on paper, freedom of choosing solvers and time-stepping algorithms and also enables low-level optimisation the implementation.

As mentioned in Section 3.1.1, the domain is discretised in the reference domain $\Omega_r$. Since the reference domain for the cable is simply

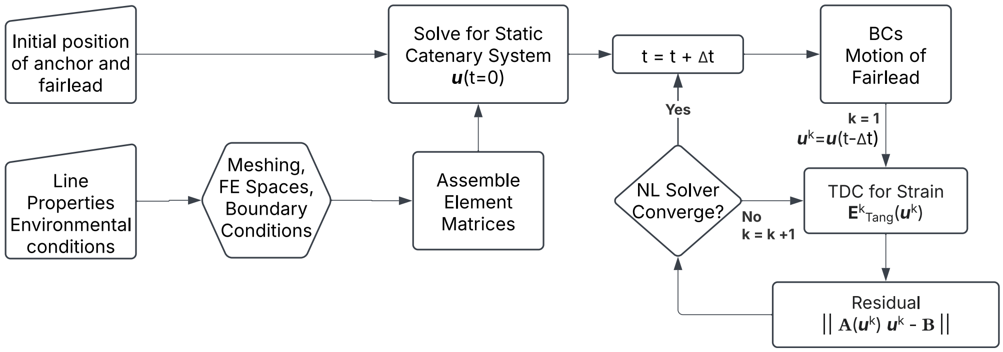


**Fig. 4.** Flowchart summarising the algorithm of the numerical model GNL-FEM.

a straight line, the meshing process for each line is straightforward regular grid along 1-dimensional line.

The next step is to define the un-deformed configuration $\Gamma_X$. In this manuscript, this is defined either as a straight line or as a parabola of length $L_0$, with the end-point at the initial position of anchor $\boldsymbol{X}_{AN}$ and the fairlead $\boldsymbol{X}_{FL}$.

Following this, we first solve for the static problem of initialising the line. This means calculating the initial displacement field $\boldsymbol{u}(t=0)$ such that the line satisfies the initial equilibrium, including the impact of self-weight, buoyancy and sea-bed. This is achieved by assembling the weak form Eq. (48) and setting all dynamic terms to zero. The resulting non-linear system is solved iteratively using a Newton–Raphson solver.

After obtaining the initial displacement field $\boldsymbol{u}(t=0)$, the dynamic problem can be solved. In this manuscript, dynamic excitation is introduced through the motion of the fairlead $\boldsymbol{u}_{FL}$, while also accounting for non-linear and dynamic forces from the sea-bed, self-drag, and wave action. Alternatively, dynamic excitation can also be applied using boundary forces via a Neumann-type boundary condition, as described in Eq. (30). The dynamic excitation disturbs the equilibrium of the line, necessitating the computation of a new displacement field that satisfies the updated equilibrium. This is achieved by assembling the weak form Eq. (48), including the dynamic terms, and solving the resulting nonlinear system iteratively using a Newton–Raphson solver. The obtained displacement field is then used to post-process the strain and stress fields using the geometric and differential quantities obtained from TDC. A summary of the solution procedure is presented in the flowchart Fig. 4. We refer to the numerical model described in this manuscript as GNL-FEM.

### 3.2. Analytical model

A fast computing analytical model is developed by means of the Lagrangian formalism Eq. (32) to solve the taut vertical line problem. This approach gives the possibility to examine multiple scenarios in short computational time, allowing for a statistical approach analysis in the design phase in floating offshore. Additionally, the analytical model can be used to validate the proposed numerical model in the ranges where the analytical model is applicable. To derive the equations of motion of an elastic cable from first principles, the kinematic Eq. (37) and constitutive relations Eq. (38) are first established. To this end, a cable of length $L_0$, and cross-section $A$ is considered. To solve the EoM Eq. (27), the method of the Galerkin decomposition is used. The solution is sought in the following form

$$u(\boldsymbol{X},t) = \sum_{m=1}^{M} U_m(\boldsymbol{X})\phi_m(t) + U_0(\boldsymbol{X})\sin(\omega t), \tag{49}$$

$$w(\boldsymbol{X},t) = \sum_{n=1}^{N} W_n(\boldsymbol{X})\psi_n(t) + W_0(\boldsymbol{X}), \tag{50}$$

**Table 1**
Properties of the vertical taut mooring line.

| Property | | Value |
|---|---|---|
| Mass per unit length | $\rho_0 A$ | $14.145\ \mathrm{kg\,m^{-1}}$ |
| Axial Stiffness | $EA$ | $10\ \mathrm{MN}$ |
| Unstretched length | $L_0$ | $100\ \mathrm{m}$ |
| Cross-section Area | $A$ | $0.01\ \mathrm{m^2}$ |
| Anchor position | $\boldsymbol{x}_{AN}$ | $(0.0, 0.0)\ \mathrm{m}$ |
| Fairlead position | $\boldsymbol{x}_{FL}$ | $(0, L_0 + \epsilon L_0)\ \mathrm{m}$ |

where $\psi_n(t)$ and $\phi_m(t)$ are the time-dependent generalised coordinates, and $U_m(\boldsymbol{X})$ and $W_n(\boldsymbol{X})$ are admissible functions in the Galerkin method, that satisfy the linear equation

$$W_n'' + \alpha_n^2 W_n = 0, \tag{51}$$

and the boundary conditions. Furthermore, $U_0(\boldsymbol{X})$ and $W_0(\boldsymbol{X})$ must satisfy the initial condition and the time-dependent boundary conditions on the domain boundaries.

For the vertical taut line case described in Section 2.6, these functions are defined as $U_m(\boldsymbol{X}) = \sin(m\pi \frac{X}{L_0})$ and $W_n(\boldsymbol{X}) = \sin(n\pi \frac{Z}{L_0})$, thereby representing $M$ modes in the transverse and $N$ modes in the in-line direction. The initial displacement is prescribed via $U_0(\boldsymbol{X}) = a_p \frac{Z}{L_0}$ and $W_0 = \epsilon_0 Z$.

By substituting Eqs. (49) and (50) into Eq. (39), multiplying both sides of the equation by $U_j(\boldsymbol{X})$ and $W_j(\boldsymbol{X})$ and integrating the resultant over $\Gamma_X$ the following equations are obtained,

$$\begin{aligned}\int_{\Gamma_X}\Bigg(\begin{bmatrix} U_j \\ W_j \end{bmatrix}^T \Bigg(\rho_0 \begin{bmatrix} \ddot{u} \\ \ddot{w} \end{bmatrix} \\ - \mu \begin{bmatrix} u''w'\left(w'+2\right) + 2u'\left(w'+1\right)w'' + 3u'^2u'' \\ u'^2w'' + 2u'u''\left(1+w'\right) + \left(3w'^2w'' + 6w'w'' + 2w''\right) \end{bmatrix} \\ - \begin{bmatrix} B_1 \\ B_2 \end{bmatrix}\Bigg)\Bigg)\, d\Gamma \\ = \int_{\Gamma_X}\left(\begin{bmatrix} 0 \\ 0 \end{bmatrix}\right) d\Gamma\end{aligned} \tag{52}$$

Eq. (52) are the equations corresponding to a reduced order model of longitudinal and transverse vibration of initially deformed cable with Dirichlet boundary conditions. The reduced order model includes a set of non-linear ordinary differential equations ($m = 1, 2, 3, \ldots, M$ and $n = 1, 2, 3, \ldots, N$) including the time functions $\phi_m(t)$ and $\psi_n(t)$, which are solved via numerical time integration by means of the fourth order Runge–Kutta integration scheme. We refer to the analytical model presented here as GNL-ANA.

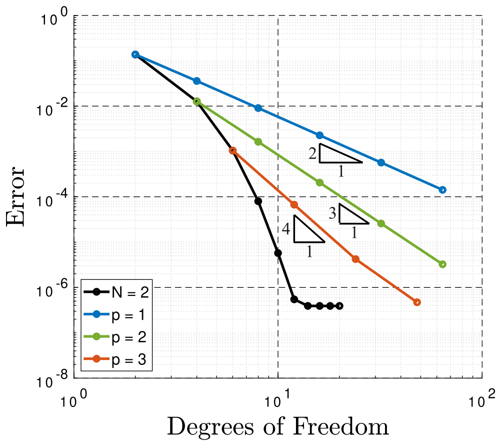


**Fig. 5.** Plots showing the computed $L^2$ error as a function of the number of degrees of freedom.

## 4. Results and discussions

### 4.1. GNL-FEM convergence analysis

The convergence characteristics of the numerical model are demonstrated using the simplified problem of taut vertical mooring line as defined in Fig. 3 in Section 2.6. We consider a line of undeformed length $L_0 = 100\,\mathrm{m}$, cross-section area $A = 0.01\,\mathrm{m}^2$, with hypothetical material properties $EA = 10\,\mathrm{MN}$ and $\rho_0 A = 14.145\,\mathrm{kg\,m^{-1}}$, as listed in Table 1. This gives a reference domain $r \in [0, 100]\,\mathrm{m}$, resulting in the undeformed configuration $\boldsymbol{X}$, where the anchor is at $\boldsymbol{X}_{\mathrm{AN}} = \boldsymbol{X}(r = 0) = [0, 0]^T$ and the fairlead is at $\boldsymbol{X}_{\mathrm{FL}} = \boldsymbol{X}(r = L_0) = [0, 100]^T$.

We first study the spatial convergence of the model by initialising the line with a initial displacement field $\boldsymbol{u}_0(r) = [a_p \sin(\pi r/L_0),\, \epsilon_0 r]^T$, where $a_p = 0.1\,\mathrm{m}$ and $\epsilon_0 = 0.01$. The boundary conditions at the anchor and the fairlead are maintained as $\boldsymbol{u}_{AN} = \boldsymbol{u}_{FL} = [0,\,0]^T$. This initial condition corresponds to axially stretching the line followed by applying a transverse displacement at its midpoint. Upon release, the line undergoes oscillations. We simulate the dynamic problem with a time-step of $10^{-6}$ s to minimise the impact of the time-step on the numerical error. Through this simplified setup we aim to study the $h$-refinement (mesh size) and $p$-refinement (order of basis function) for the numerical model. We investigate the setup with number of elements $N = 2$ while varying $p \in [1, 10]$; linear element $p = 1$ with $N \in \{2, 4, 8, 16, 32, 64\}$; quadratic element $p = 2$ with $N \in \{2, 4, 8, 16, 32\}$; and cubic element $p = 3$ with $N \in \{2, 4, 8, 16\}$. The error is reported after 1000 time-steps using the $L^2$ norm error= $\|\boldsymbol{u} - \boldsymbol{u}_{\mathrm{ref}}\|_{L^2} = \sqrt{\int_{\Omega_r} |\boldsymbol{u} - \boldsymbol{u}_{\mathrm{ref}}|^2}$, where $\boldsymbol{u}_{\mathrm{ref}}$ is the numerical solution obtained using $N = 320$ and cubic polynomial basis function. The result in Fig. 5 showcases an expect $p + 1$ rate of convergence for a given $p$ order polynomial basis function.

We further study the $h$-refinement characteristics by simulating a dynamic problem with an accelerating fairlead boundary. For this analysis, the dynamic displacement at the fairlead is defined as $\boldsymbol{u}_{\mathrm{FL}} = [a_p \sin(2\pi f_p t),\, \epsilon_0 L_0]^T$, where $a_p = 0.1\,\mathrm{m}$, $f_p = 0.8\,\mathrm{Hz}$ and the initial axial stretch of the line is $\epsilon_0 = 0.01$. For the convergence analysis, we will excite the line via the fairlead and compare the results after two excitation cycles $T_{\mathrm{end}} = 2/f_p$. Analytically, the linear $n$th natural frequencies of a stretched string is given by

$$f_n = \frac{n}{2L_0}\sqrt{\frac{EA\epsilon_0}{\rho_0 A}} \tag{53}$$

Therefore, for this particular line configuration having $\epsilon_0 = 0.01$, the first two linear natural frequencies are $f_1 = 0.42\,\mathrm{Hz}$ and $f_2 = 0.84\,\mathrm{Hz}$. Consequently, an excitation at $f_p = 0.8\,\mathrm{Hz}$ should induce significant response in the string.

A small time-step of $\Delta t = 1/(500 f_p)$ is maintained for all spatial convergence tests to minimise the influence of the time-step on the analysis. The spatial convergence is examined by varying both the number of mesh elements and the order of the polynomial basis function. The number of elements varies in the range $N_{\mathrm{ele}} \in \{10, 20, 40, 80, 160\}$. We study the convergence for linear $p = 1$, quadratic $p = 2$ and cubic $p = 3$ polynomial basis functions. The error is reported after two excitation cycles $T_{\mathrm{end}} = 2/f_p$ using the $L^2$ norm error, where $\boldsymbol{u}_{\mathrm{ref}}$ is the numerical solution obtained using $N_{\mathrm{ele}} = 320$ and cubic polynomial basis function. Fig. 6a reports the computed error obtained using the different number of elements and the different polynomial basis functions. The plot also overlays the analytical polynomial functions of order $p + 1$, thereby demonstrating an order $O(p + 1)$ rate of convergence when using a polynomial basis function of order $p$. Fig. 6b presents the plot of the horizontal displacement $u(r)$ obtained using linear polynomial basis function and four different mesh sizes, further qualitatively demonstrating the convergence of We also study time-step convergence by repeating the analysis using $N_{\mathrm{ele}} = 2000$, $p = 1$ to minimise the influence of the mesh on the results. The time-step is varied as $T/\Delta t \in \{10, 20, 40, 80, 160\}$ and the $L^2$ norm error is computed using $T/\Delta t = 320$ as the reference. Fig. 7a demonstrates a 2nd order rate of convergence as expected from the Generalised-$\alpha$ time-stepping scheme. Fig. 7b overlays the solution obtained using the different time-steps.

### 4.2. GNL-FEM verification: Parabolic hanging line static

We move on to a more complex test case, involving the combined effects of an external body force and a more comprehensive 2D configuration. We examine an elastic rope in a 2D space, suspended between two fixed points and subject to gravitational sagging. This test case serves as a validation benchmark for the formulation of the static problem.

The rope is suspended between points $\boldsymbol{X}_1 = (0, 0.5)\,\mathrm{m}$ and $\boldsymbol{X}_2 = (1.0, 0)\,\mathrm{m}$. The rope has a cross-sectional area of $A = 0.01\,\mathrm{m}^2$, Young's modulus $E = 10^4\,\mathrm{Pa}$, Poisson's ratio $\nu = 0$, and hence the corresponding Lamé constants $\lambda = 0$ and $\mu = E/2$. The initial undeformed configuration of the rope is defined in a reference domain $r \in [0, 1]$ as follows and is shown in Fig. 8 as $\Gamma_{\boldsymbol{X}}$.

$$\boldsymbol{X}(r) = \begin{bmatrix} r \\ \frac{1}{2}(1 - r) - \frac{1}{7}\sin(\pi r) \end{bmatrix} \tag{54}$$

The external body force per unit volume of the rope due to the action of the gravity is taken as $\boldsymbol{B}(\boldsymbol{X}) = [0, 2000]^T\,\mathrm{N\,m^{-3}}$. We formulate the finite-element problem using 500 elements with second order polynomial basis function. The initial length of the undeformed $\Gamma_{\boldsymbol{X}}$ curve is $L_0(\Gamma_{\boldsymbol{X}}) = 1.1540019835742\,\mathrm{m}$. Under the action of the external force, the line undergoes sagging and deforms to $\Gamma_{\boldsymbol{x}}$ with a length of $L(\Gamma_{\boldsymbol{x}}) = 1.2755932022498\,\mathrm{m}$. The elongation of the line is $L(\Gamma_{\boldsymbol{x}})/L_0(\Gamma_{\boldsymbol{X}}) = 1.1053648264096$ and has a stored potential energy of $= 0.7528302282958\,\mathrm{N\,m}$. Fig. 8 shows the plot of the deformed configuration $\Gamma_{\boldsymbol{x}}$, along with the contour plots of the principal Cauchy stress in the line. For validation, we benchmark our results against previous numerical results from Fries and Schöllhammer (2020), which reported an elongation of 1.1053648264108 and the stored potential energy $= 0.7528302283000\,\mathrm{N\,m}$. The difference in the results is smaller that $10^{-9}$%. Additionally Fig. 8 also shows the deformed configuration reported by Fries and Schöllhammer (2020), which overlaps closely with $\Gamma_{\boldsymbol{x}}$ obtained from our model.

### 4.3. Case study: Hardening behaviour of taut vertical line

In this section, we continue the investigation of the harmonic transverse excitation of a taut vertical line, as outlined in Fig. 3 in Section 2.6. We employ the numerical and the analytical solution approaches. In this particular case study, we neglect body forces. To

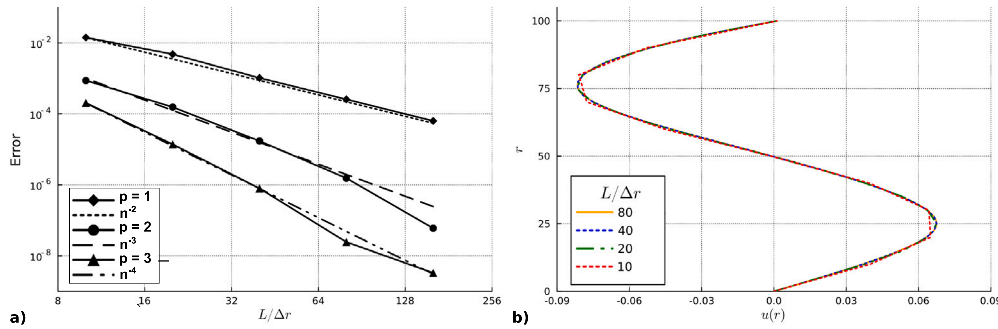


**Fig. 6.** (a) Plots showing the computed numerical error with the increasing number of elements, using elements of polynomial degree $p = 1, 2, 3$. (b) Plots showing the horizontal displacement field $u(r)$ at the end of two excitation cycles, obtained using different number of mesh elements and linear polynomial basis function $p = 1$.

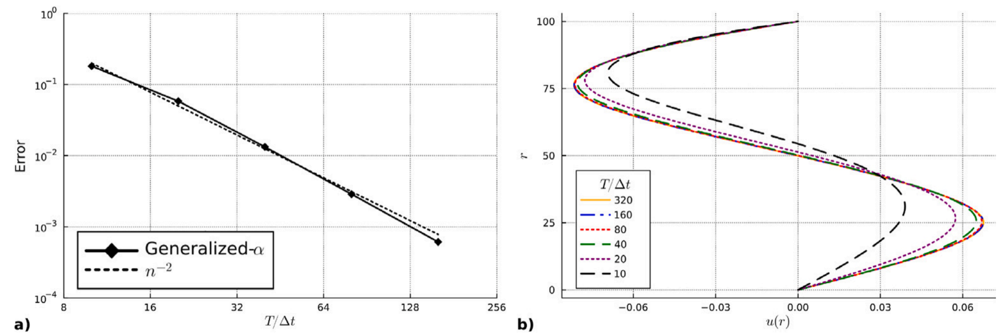


**Fig. 7.** (a) Plots showing the computed numerical error with the increasing time-step resolution. (b) Plots showing the horizontal displacement field $u(r)$ at the end of two excitation cycles, obtained using different time-step resolution.

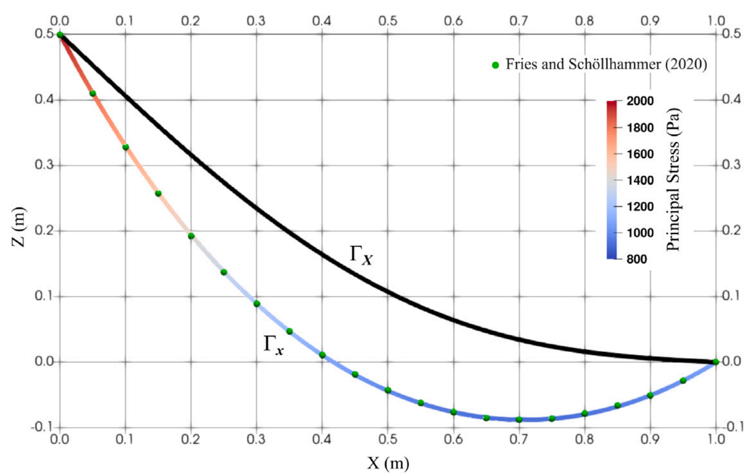


**Fig. 8.** Plot showing the initial un-deformed configuration $\Gamma_X$ and the deformed shape $\Gamma_x$ of the line under the action of gravity. The green points are the deformed shape of the line as reported in Fries and Schöllhammer (2020). The deformed shape $\Gamma_x$ is also coloured with the value of the local principal stress.

facilitate the parametric study, we focus on a hypothetical mooring line with properties specified in Table 1. The key findings in this section are presented in terms of normalised frequency $f_p/f_1$, and are therefore relevant to a broader range of taut mooring systems.

#### 4.3.1. Results from GNL-FEM

Following the convergence analysis, we use a mesh with $N_{\text{ele}} = L_0/\Delta r = 100$ and quadratic polynomial basis function. The time-step for each test case is set to $\Delta t = 1/(100 f_p)$. Each simulation runs for 200 excitation cycles, ensuring that the signal is long enough to produce an accurate spectrum for analysis. Finally, in order to minimise noise induced by a sudden onset of the fairlead excitation, the amplitude of the excitation is ramped up over ten wave periods $T_{\text{ramp}} = 10/f_p$. For this setup, the model takes about 70 ms per time-step, which translates into about 24 min for simulation 200 excitation cycles, using a serial run on system with 11th Gen Intel(R) Core(TM) i5-11320H @ 3.20 GHz processor and 16 GB RAM.

Let us consider a small axial strain $\epsilon_0 = 0.01$, small oscillation amplitude $a_p = 0.1$ m. This is a small displacement scenario, with first four linear natural frequencies $f_{1,2,3,4} = \{0.42, 0.84, 1.26, 1.68\}$ Hz as per Eq. (53). We monitor the principal strain $E_1$ at the fairlead over time. For the vertical taut line, this is given by

$$E_1 = w' + \frac{1}{2}\left(u'^2 + w'^2\right) \tag{55}$$

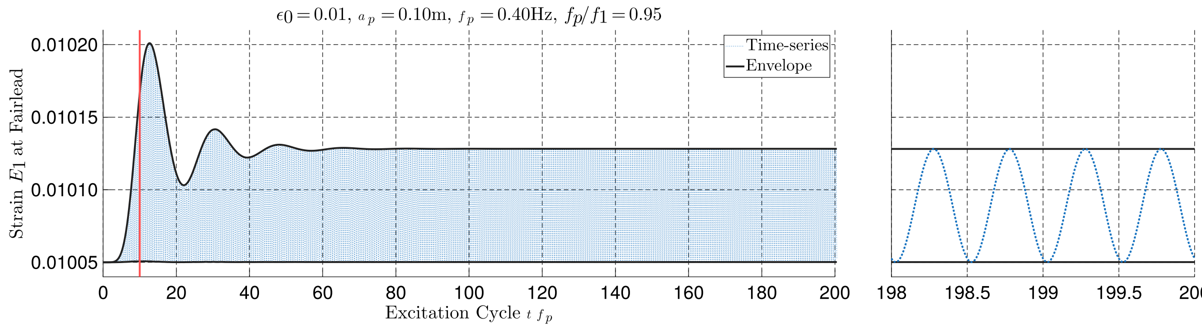


**Fig. 9.** Plot of principal strain $E_1$ time-series and its peak envelope, at the fairlead for $\epsilon_0 = 0.01$, $a_p = 0.10\,\mathrm{m}$, $f_p = 0.40\,\mathrm{Hz}$.

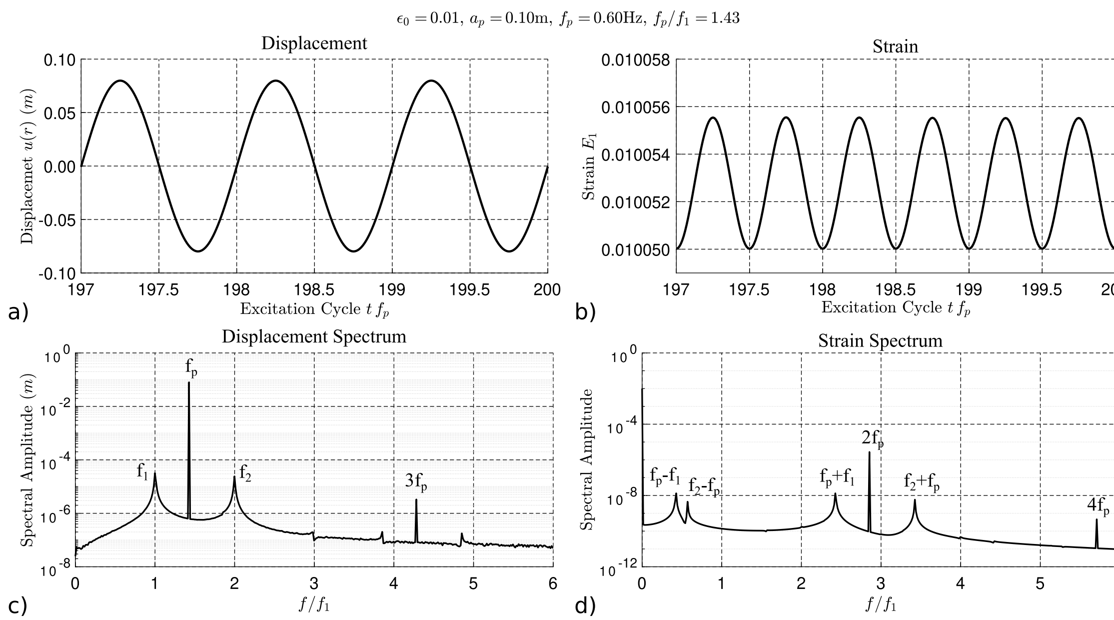


**Fig. 10.** Plots of GNL-FEM results for displacement $u(r)$ and principal strain $E_1$ at a point ($r = 0.9L_0$), for $\epsilon_0 = 0.01$, $a_p = 0.10\,\mathrm{m}$, $f_p = 0.60\,\mathrm{Hz}$. (a) Displacement $u(r)$ time-series. (b) Principal strain $E_1$ time series. (c) Displacement $u(r)$ spectrum. (d) Principal strain $E_1$ spectrum.

given the strain tensor Eq. (37). We introduce a small amount of dissipation in the system using drag forcing with $C_d = 0.01$. For frequencies away from the natural frequencies, this small dissipation has negligible impact on the results. However, for excitation near the natural frequency, this dissipation helps to filter out the presence of spurious frequencies and achieve a steady-state in the response.

Fig. 9 presents the time-series of the principal strain at the fairlead ($r = L_0$) for the scenario $\epsilon_0 = 0.01$, $a_p = 0.10\,\mathrm{m}$, $f_p = 0.40\,\mathrm{Hz}$. The signal starts with the principal strain $E_1 = 0.01005$ as a result of the static equilibrium. Following this the amplitude of the fairlead excitation is gradually ramped up for 10 excitation cycles, as indicated by the vertical line in Fig. 9. Since the excitation frequency $f_p$ is close to the first linear natural frequency $f_1$, we observe a significant transient response due to the excitation of the system's natural modes. This transient response is gradually damped out by the small amount of damping introduced via drag forcing. Once this damping effect stabilises the system, a steady-state response is achieved. Our analysis focuses primarily on this steady-state behaviour. For excitation frequencies further from the natural frequency, the transient response would be less pronounced and would damp out more quickly. We conduct the frequency analysis for the last 100 excitation cycles. A zoomed in view of the $E_1$ time series for the final two excitation cycles is also shown in Fig. 9.

Let us consider a scenario where the excitation frequency is not near the linear natural frequencies. We analyse the case with parameters $\epsilon_0 = 0.01$, $a_p = 0.10\,\mathrm{m}$, and $f_p = 0.60\,\mathrm{Hz}$, which corresponds to a ratio of $f_p/f_1 = 1.43$. This prescribed frequency lies between the first and second linear natural frequencies, $f_1$ and $f_2$. We study a point $r = 0.9L_0$, located near the fairlead. The steady-state time-series and corresponding spectrum of the displacement $u(r)$ at this location are shown in Fig. 10a,c, while the principal strain $E_1$ is presented in Fig. 10b,d. The spectrum of the displacement field shows the presence of the prescribed frequency $f_p$, along with contributions from the natural frequencies $f_1$ and $f_2$. We also see a strong presence of $3f_p$, which arises from the non-linear term $u'^2u''$ in Eq. (39). Since the principal strain, as described by Eq. (55) contains quadratic terms with respect to the displacement field, the strain spectrum in Fig. 10d clearly shows the presence of corresponding sub and super harmonics, including the difference frequencies $f_p - f_1$, $f_2 - f_p$ and the sum frequencies $f_p + f_1$, $f_p + f_2$ and $2f_p$.

We repeat the analysis for four frequencies $f_p/f_1 = \{0.48., 0.95, 1.43, 1.90\}$, and now monitor the principal strain at the fairlead $r = L_0$. Fig. 11 shows the steady state time-series of $E_1$ at fairlead ($r = L_0$), along with its spectrum for these excitation frequencies. From Fig. 11 we draw a few observations. Firstly, for low excitation frequencies $f_p/f_1 < 1$, the response of the cable is predominantly quasi-static. This is evident from the strain spectrum, where we observe a sharp peak at $2f_p/f_1$ while the other harmonics have very low amplitudes. The response for $f_p/f_1 = 1.43$ shows clear peaks at $2f_p/f_1$, the neighbouring natural frequencies $f_1$ and $f_2$, and the corresponding sub and super

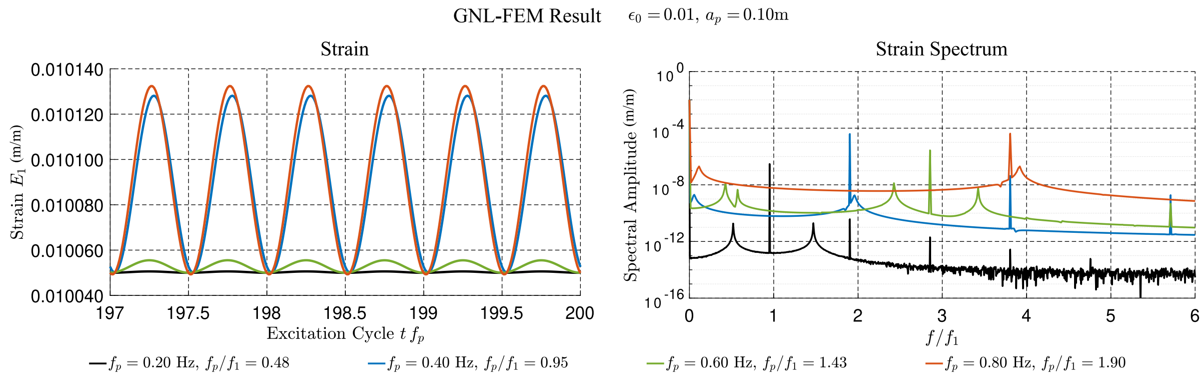


**Fig. 11.** Plots of GNL-FEM results on principal strain $E_1$ at the fairlead ($r = L_0$) for $\epsilon_0 = 0.01$, $a_p = 0.10\,$m, $f_1 = 0.42\,$Hz, $f_p = \{0.2, 0.4, 0.6, 0.8\}\,$Hz (a) $E_1$ time-series. (b) $E_1$ spectrum.

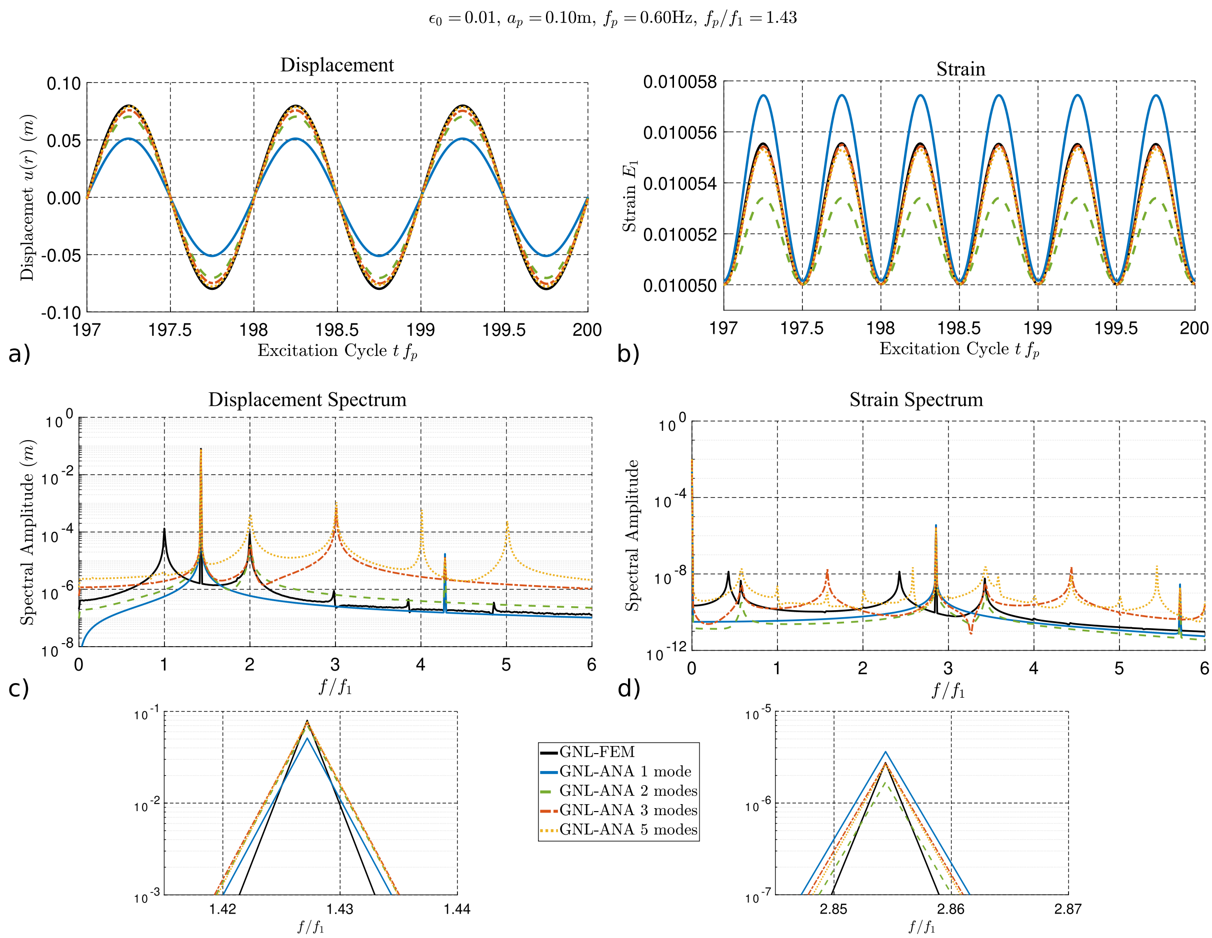


**Fig. 12.** Plots of GNL-FEM and GNL-ANA results for displacement $u(r)$ and principal strain $E_1$ at a point ($r = 0.9L_0$), for $\epsilon_0 = 0.01$, $a_p = 0.10\,$m, $f_p = 0.60\,$Hz. (a) Displacement $u(r)$ time-series. (b) Principal strain $E_1$ time series. (c) Displacement $u(r)$ spectrum. (d) Principal strain $E_1$ spectrum.

harmonics. As the excitation frequency approaches the linear natural frequencies, such as $f_p/f_1 = \{0.95, 1.90\}$, we observe a high-magnitude peak at $2f_p/f_1$, along with significant response also at the nearest sub-harmonic $f_n - f_p$ and the super-harmonics $f_p + f_n$ and $2f_p$. This behaviour aligns with the expected amplification of the response in the vicinity of the system's natural frequency.

#### 4.3.2. Results from GNL-ANA

We now employ the analytical approach to solve the taut vertical line problem for two main reasons. First, we aim to determine the number of modes or parameters necessary to obtain a solution using this method. Second, we assess the feasibility of using the analytical approach as a reduced-order alternative. This would allow GNL-ANA to be utilised for conceptual design and optimisation, while GNL-FEM would be reserved for comprehensive dynamic analysis.

As outlined in Section 3.2, the analytical solution is constructed using $M$ sinusoidal modes in the transverse direction and $N$ sinusoidal modes in the in-line direction. Traditionally, analytical solutions for such problems are sought in the vicinity of the first mode. However, in this study, we examine the impact of incorporating varying numbers of modes.

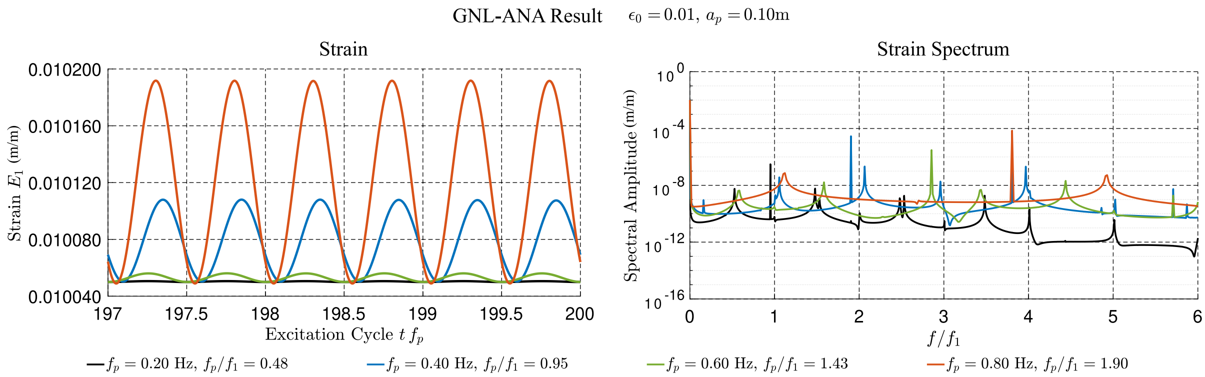


**Fig. 13.** Plots of GNL-ANA results on principal strain $E_1$ at the fairlead ($r = L_0$) for $\epsilon_0 = 0.01$, $a_p = 0.10$ m, $f_1 = 0.42$ Hz, $f_p = \{0.2, 0.4, 0.6, 0.8\}$ Hz (a) $E_1$ time-series. (b) $E_1$ spectrum.

We consider cases with one mode $M, N = 1$, two modes $M, N = 2$, three modes $M, N = 3$ and five modes $M, N = 5$. We add a small amount of quadratic damping in the analytical solution for achieving the steady state quicker, similar to the numerical model. The test is conducted for $\epsilon_0 = 0.01$ and $a_p = 0.10$ m, with an excitation frequency of $f_p/f_1 = 1.43$. Fig. 12 presents the displacement and principal strain $E_1$ at $r = 0.9L_0$, located near the fairlead. The figure compares the time-series and their spectra, obtained from GNL-FEM with those from GNL-ANA, considering $M, N = 1$, $M, N = 2$, $M, N = 3$ in the transverse direction. The time-step for RK4 scheme used in the analytical solution procedure is $\Delta t_{\text{GNL-ANA}} = 10^{-3}$ s.

From Fig. 12, several observations can be made regarding the analytical and numerical solutions for the line's response at an excitation frequency between the first and second modes ($f_p/f_1 = 1.43$). GNL-ANA with a single mode ($M, N = 1$) underestimates the peak displacement while overestimating the peak strain compared to GNL-FEM. As the number of modes increases to $M, N = 5$, the analytical solution from GNL-ANA gradually converges to the GNL-FEM solution in the time domain for both displacement and principal strain $E_1$. Additionally, the displacement and strain spectra show that GNL-ANA approaches the GNL-FEM amplitude at the excitation frequency $f_p$ and at $3f_p$(which arises from the $u'^2u''$ nonlinearity).

Similar to the tests from GNL-FEM in the previous section, we repeat the study for four discrete frequencies $f_p/f_1 = \{0.48., 0.95, 1.43, 1.90\}$ and monitor the principal strain $E_1$ time-series and its spectra at the fairlead $r = L_0$, as reported in Fig. 13. For these tests we consider 5 modes, i.e., $M, N = 5$ for minimising the errors the amplitude of the excitation frequency response for high frequency scenarios.

In general, the analytical solution captures the main features at all frequencies, as reported in Section 4.3.1. However, we see a number of extra peaks in the analytical response, corresponding to the 5 modes considered in the analysis. Furthermore, when compared to the GNL-FEM results in Fig. 11, the analytical solution exhibits greater noise, as indicated by the higher amplitude at non-peak frequencies. These discrepancies in the GNL-ANA results are due to the fewer degrees of freedom in GNL-ANA (dofs = 10 for $M, N = 5$) compared to GNL-FEM (dofs = 200 for 100 quadratic elements), and the difference in numerical damping resulting from the Generalised-$\alpha$ time-stepping scheme for GNL-FEM and the Runge–Kutta 4th-order time-stepping scheme for GNL-ANA.

The peak values at $2f_p$ obtained from GNL-ANA and GNL-FEM in Figs. 11 and 13 are presented in Table 2. The results indicate a reasonable agreement between GNL-ANA with ($M, N = 5$) and GNL-FEM, with the error increasing as the excitation frequency rises. Increasing the number of modes in GNL-ANA would further reduce this error.

#### 4.3.3. Frequency sweep results from GNL-FEM and GNL-ANA

The first test is done for low pre-tension low excitation amplitude case $\epsilon_0 = 0.01$, $a_p = 0.10$ m having first linear natural frequency at $f_p = 0.42$ Hz. The principal strain $E_1$ amplitude at $2f_p$ obtained from GNL-FEM and GNL-ANA for $f_p/f_1 \in (0, 7)$ are plotted in Fig. 14a and c, respectively. Additionally, the results from both methods are overlaid in Fig. 15a for comparison. The GNL-FEM results reveal several key observations. At frequencies $f_p/f_1 < 0.5$, the response is nearly quasi-static, where the response amplitude is nearly independent of the excitation frequency. As the excitation frequency approaches the system's natural frequencies, there is a noticeable amplification in response amplitude. The response peaks occur at $f_p/f_1 = 1.01$ for the first mode, $f_p/f_1 = 2.02$ for the second mode, $f_p/f_1 = 3.09$ near the third mode, and $f_p/f_1 = 4.16$ near the fourth mode. Notably, as the frequency increases, the response peak shifts further from the nearest linear natural frequency. This shift indicates non-linear hardening, where the natural frequency of the line increases with rising excitation frequency.

In order to investigate the influence of the excitation amplitude, we study the cases with $\epsilon_0 = 0.01$ and $a_p \in \{0.10, 0.20, 0.40, 0.80\}$ m. The results from GNL-FEM and GNL-ANA for these cases are presented in Fig. 14a and c, respectively. Additionally, for $a_p = 0.80$ m, the results from both methods are overlaid in Fig. 15a for comparison. From the GNL-FEM results, we draw a few observations. The increase in amplitude leads to a quadratic increase in the quasi-static response for low frequencies $f_p/f_1 < 0.5$. Furthermore, there is a pronounced hardening or right shift of the natural frequency with the increase in the excitation amplitude.

Finally, we examine the effect of pre-tension or pre-stretch in the line by considering the case with $\epsilon_0 = 0.04$, where the first linear natural frequency is $f_1 = 0.84$ Hz, as given by Eq. (53). A frequency sweep is performed for $f_p/f_1 \in (0, 7)$. The results obtained from GNL-FEM and GNL-ANA for excitation amplitudes $a_p \in \{0.10, 0.20, 0.40, 0.80\}$ m are presented in Fig. 14b and d, respectively. Additionally, Fig. 15b overlays the results from both methods for $a_p = 0.8$ m. With increased pre-tensioning, the quasi-static response for $f_p/f_1 < 0.5$ remains largely unaffected. Moreover, the rightward shift in the natural frequency due to increasing excitation amplitude and frequency becomes less pronounced as pre-tensioning increases. In the high pre-tensioning scenario, the GNL-FEM solution exhibits a peak in response at $f_p/f_1 = 2.62$, which is observed across all excitation amplitudes. The underlying physical reason for this peak remains unclear at present. However, it is likely associated with the nonlinear terms proportional to $w'$ in Eq. (39). Infact, the GNL-ANA results indicate the presence of a peak around $f_p/f_1 = 2.62$, as seen in Fig. 14d.

Overall, the GNL-ANA results exhibit a response similar to that of GNL-FEM, with the response magnitude and peak frequencies aligning well up to the second mode across all tests. Beyond this point, deviations between the GNL-ANA and GNL-FEM results become apparent. However, we still observe the right shift of the natural frequency of the system with increase in excitation frequency and the excitation amplitude. These results highlight that for low excitation frequencies

**Table 2**
Amplitude of principal strain at frequency $2f_p$ at the fairlead ($r = L_0$).

| Excitation frequency $f_p$(Hz) | $f_p/f_1$ | Amplitude of $E_1$ at $2f_p$ GNL-FEM | Amplitude of $E_1$ at $2f_p$ GNL-ANA | Comparison $\left\lvert\frac{\text{GNL-ANA}}{\text{GNL-FEM}} - 1\right\rvert$ |
|---|---|---|---|---|
| 0.20 | 0.48 | $2.94 \times 10^{-7}$ | $3.04 \times 10^{-7}$ | 0.034 |
| 0.40 | 0.95 | $3.66 \times 10^{-5}$ | $3.90 \times 10^{-5}$ | 0.066 |
| 0.60 | 1.43 | $2.75 \times 10^{-6}$ | $2.51 \times 10^{-6}$ | 0.087 |
| 0.80 | 1.90 | $4.09 \times 10^{-5}$ | $3.57 \times 10^{-5}$ | 0.127 |

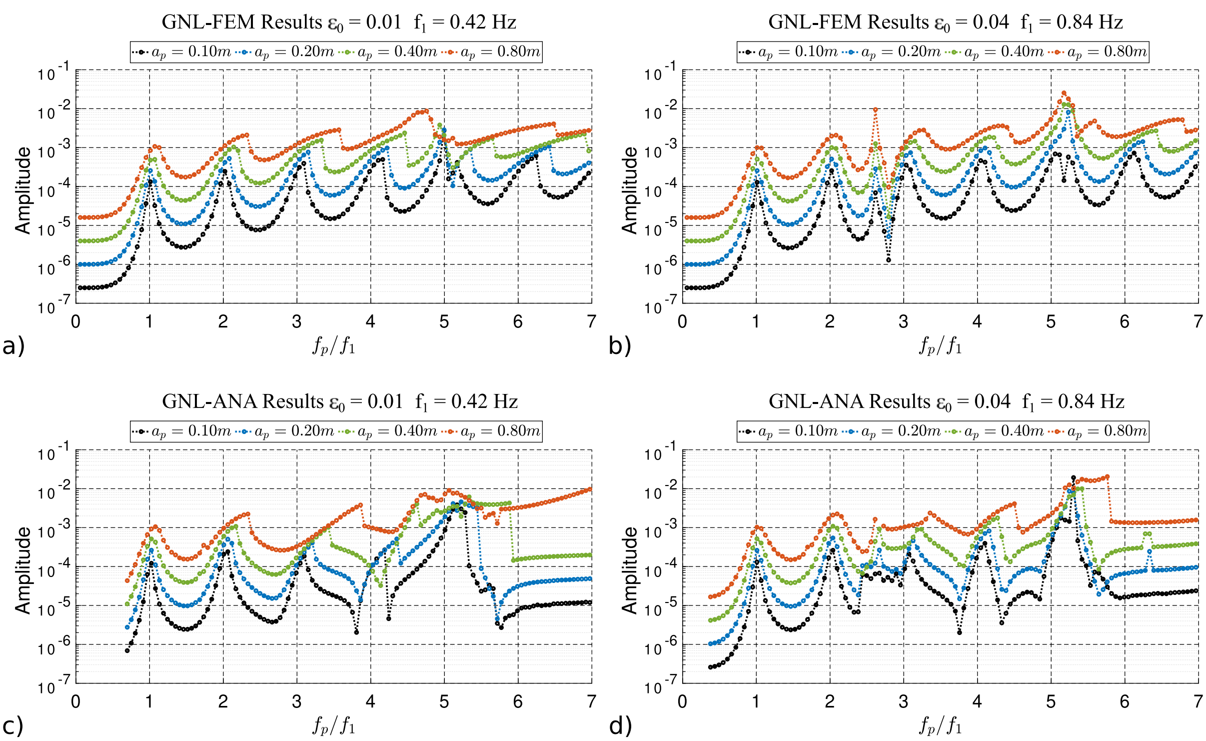


**Fig. 14.** Frequency sweep results showing the amplitude of the principal strain $E_1$ at frequency $2f_p$ as a function of the excitation frequency $f_p$ over the range $f_p/f_1 \in (0, 7)$. (a) GNL-FEM results for $\epsilon_0 = 0.01$. (b) GNL-FEM results for $\epsilon_0 = 0.04$. (c) GNL-ANA results for $\epsilon_0 = 0.01$. (d) GNL-ANA results for $\epsilon_0 = 0.04$.

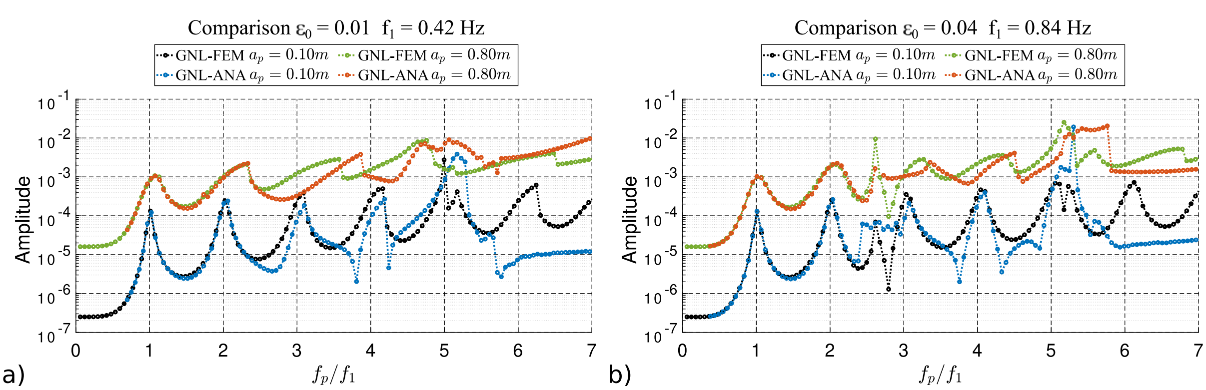


**Fig. 15.** Frequency sweep results showing the amplitude of the principal strain $E_1$ at frequency $2f_p$ as a function of the excitation frequency $f_p$ over the range $f_p/f_1 \in (0, 7)$. (a) GNL-FEM and GNL-ANA results for $\epsilon_0 = 0.01$. (b) GNL-FEM and GNL-ANA results for $\epsilon_0 = 0.04$.

(up-to the 2nd mode in the tested scenarios), the analytical approach can provide a sufficient estimation of the strains for the specific case of the vertical taut line.

The geometric hardening behaviour and harmonics observed in the present results are consistent with phenomena reported for taut bridge cable systems in the literature (Macdonald, 2016). It is also known from this literature that under purely planar harmonic excitation, the planar response can become unstable above a certain amplitude threshold, beyond which non-planar whirling motion develops (Nayfeh and Mook, 1995; Macdonald, 2016). The present 2D analysis is therefore valid within the planar response regime.

#### 4.3.4. Potential and kinetic energy, evaluated using GNL-ANA

The GNL-ANA model serves as an effective preliminary tool for analysing the response of taut mooring systems. As demonstrated in Section 4.3, the GNL-ANA model with five modes provides reasonable accuracy up to the second natural frequency of the line. This makes it a valuable tool for rapidly assessing various advanced characteristics of

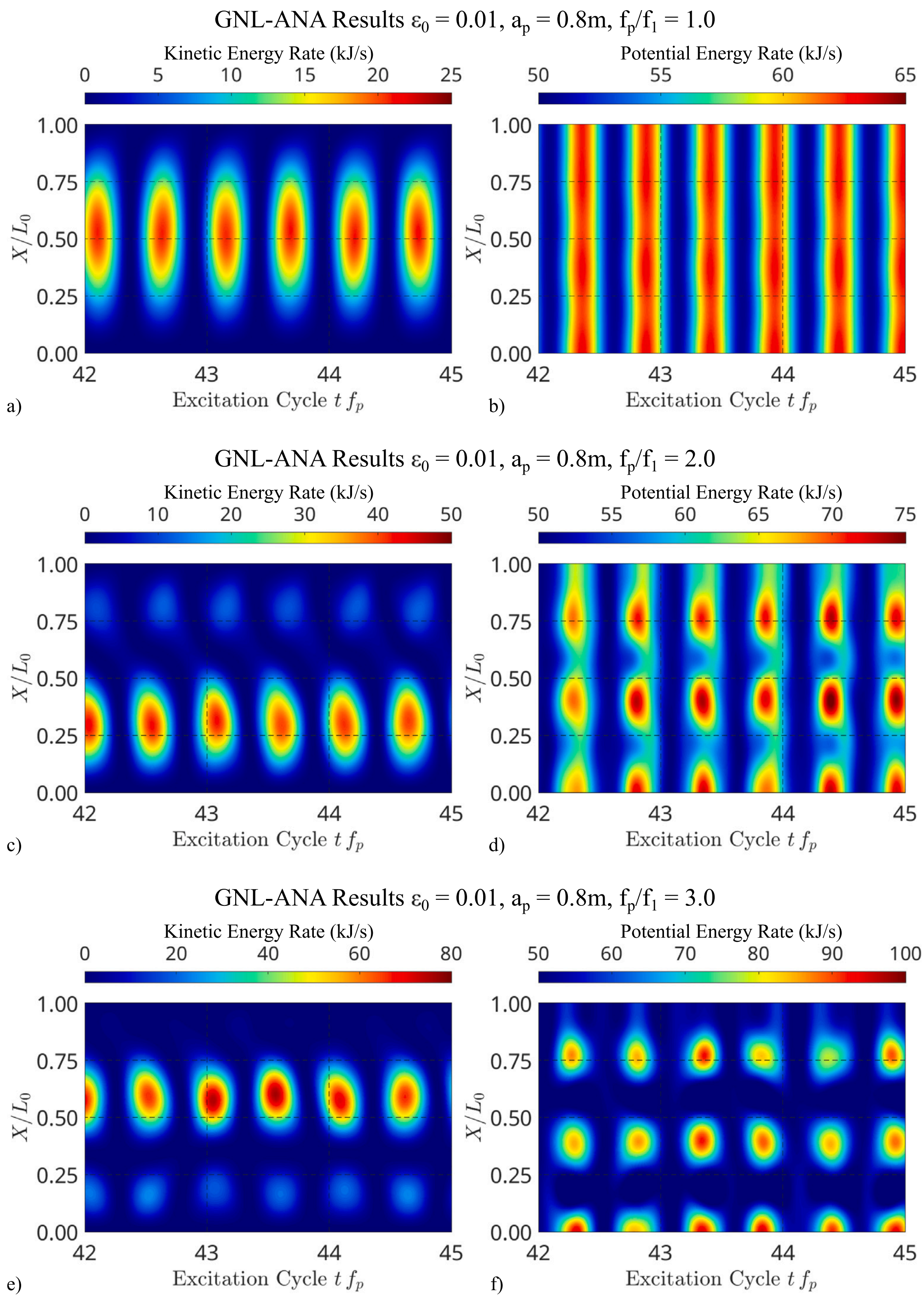


**Fig. 16.** Contour plots showing the variation of kinetic and potential energy rate along the line over time.

the system. For instance, it can be utilised to evaluate the local rate of change in potential and kinetic energy along the line. The contour plot in Fig. 16 illustrates the spatial and temporal distribution of potential and kinetic energy rates at different time instances. Although the GNL-ANA model does not currently include thermo-elastic coupling effects, the proposed energy-based visualisation provides valuable insight into regions that may act as potential temperature hotspots along the mooring line. This sets a basis for possibly exploring thermo-mechanical coupling for quantifying the temperature hotspots based on this energy distribution. This aspect is particularly important, as synthetic mooring lines subjected to dynamic loading can experience significant localised temperature increases. Such temperature elevations may alter the material properties of the line and accelerate degradation processes, ultimately increasing the risk of mechanical failure.

In Fig. 16, we present the kinetic and potential energy rates for the case $\epsilon_0 = 0.01$, $a_p = 0.8\,\mathrm{m}$, considering three excitation frequencies $f_p/f_1 \in \{1.0, 2.0, 3.0\}$. Since these frequencies are in the vicinity of the first, second, and third natural modes, the response is significantly amplified. The figures reveal two distinct peaks in the kinetic and potential energy rates per excitation cycle. Thermal energy dissipation within the line is expected to be proportional to these energy rate variations, and consequently, local temperature fluctuations will also correlate with these changes. From Fig. 16, we can observe that the peak in kinetic an potential energy rates are out of phase. However,

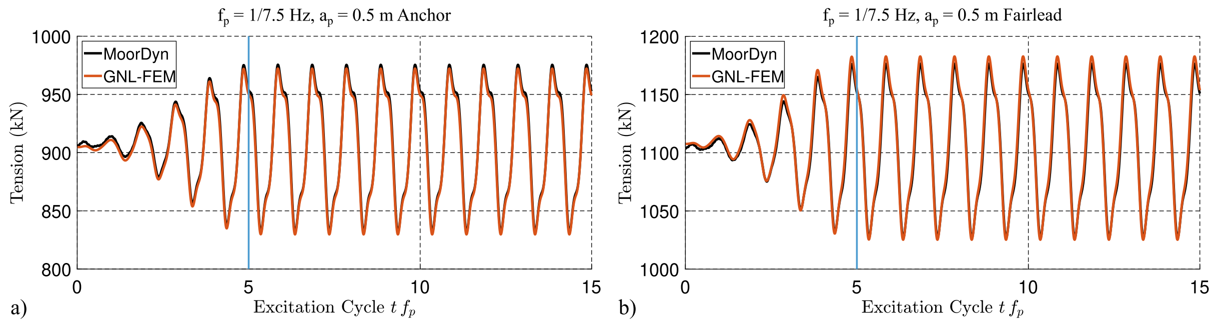


**Fig. 17.** Plots showing the tension at the fairlead and anchor, showing the simulation ramp-up until $tf_p = 5$. The results are obtained from GNL-FEM and MoorDyn for the catenary line described in Table 3, under an excitation of $f_p = 1/7.50\,\text{Hz}$ and $a_p = 0.5\,\text{m}$.

**Table 3**
Properties of chain mooring line and sea-bed from DeepCWind semi-submersible tests.

| Property | | Value |
|---|---|---|
| Nominal diameter | | 0.0766 m |
| Mass per unit length | | $113.35\,\text{kg}\,\text{m}^{-1}$ |
| Axial stiffness | $EA$ | 753.6 MN |
| Un-stretched length | | 835.35 m |
| Anchor position | $x_{AN}$ | (0.0, 0.0) m |
| Fairlead position | $x_{FL}$ | (796.7, 186.0) m |
| Normal drag coefficient | $C_{d,n}$ | 2.0 |
| Axial drag coefficient | $C_{d,t}$ | 0.4 |
| Sea-bed stiffness | $k_b$ | $3 \times 10^6\,\text{Pa}\,\text{m}^{-1}$ |
| Sea-bed damping | $c_b$ | $3 \times 10^5\,\text{Pa}\,\text{s}\,\text{m}^{-1}$ |

when analysing the variation along the line, there are specific regions where both kinetic and potential energy rates peak simultaneously. These locations may serve as potential hotspots for thermal build-up. For $f_p/f_1 = 1.0$, the hotspot is located within $X/L_0 \in (0.25, 0.75)$. For $f_p/f_1 = 2.0$, it shifts to $X/L_0 \in (0.25, 0.50)$, while for $f_p/f_1 = 3.0$, it is observed within $X/L_0 \in (0.50, 0.75)$. These findings highlight the capability of the analytical model to provide quantitative insights into the dynamic behaviour of the mooring line, facilitating a proactive and pre-emptive approach in the design process.

### 4.4. Case study: Catenary mooring line dynamic

As a final study, we study the numerical model GNL-FEM for dynamic excitation of catenary type mooring line, as sketched in Fig. 2. We compare the results obtained from GNL-FEM against MoorDyn (Hall and Goupee, 2015), which is a common used lumped-mass mooring line model.

We consider a mooring line from the DeepCWind semi-submersible tests, with the properties of the line indicated in Table 3, based on the MoorDyn input file found at OpenFAST/r-test. The line is placed in water-depth $d_0 = 200\,\text{m}$, with the anchor at the sea-bed at $x_{AN} = (0.0, 0.0)\,\text{m}$ and the fairlead at $x_{FL} = (796.7, 186.0)\,\text{m}$. We include the influence of gravity and buoyancy body forces. The sea bed is modelled as a damped spring bed, with the stiffness and the damping coefficients mentioned in Table 3. We also consider the impact of the self drag of the line, with the axial and normal drag coefficients also mentioned in Table 3. Simulations in both GNL-FEM and Moordyn have been executed with the same properties as mentioned in Table 3.

The line is meshed uniformly, with $N_{\text{ele}} = L_0/\Delta r = 100$ quadratic elements. We expose the line to dynamic excitation via the fairlead, by moving the fairlead sinusoidally along the surge (X) axis, with a prescribed frequency $f_p$ and amplitude $a_p$. For each test case, the MooDyn and GNL-FEM simulations are executed at a time-step of $\Delta t = 1/100 f_p$. We monitor the tension at the anchor ($r = 0$) and the fairlead ($r = L_0$). To prevent abrupt excitation, the amplitude is gradually increased from zero to $a_p$ over five excitation cycles, as shown in Fig. 17, which presents the time series results for the excitation case $f_p = 1/7.5\,\text{Hz}$, $a_p = 0.5\,\text{m}$. The simulations take about 5 s to run in MoorDyn, but about 460 s in GNL-FEM, owing to the Generalised-$\alpha$ time stepping and iterative Newton–Raphson solver as mentioned in Section 3.1.2

Fig. 18 presents the steady-state time series of tension at both the anchor and the fairlead for various excitation frequencies and amplitudes. The figure also provides a comparison between the results obtained from GNL-FEM and MoorDyn. To quantify the difference between the GNL-FEM and MoorDyn time series, we use the parameter $P_d = \sum \left(T_{\text{GNL-FEM}} - T_{\text{MoorDyn}}\right)^2 / \sum \left(T_{\text{MoorDyn}}\right)^2$, following the approach in Crespo et al. (2007). The computed values for $P_d$ are provided in Table 4.

From the figures and the error table, several key observations can be made. The cases with $f_p = 1/7.5\,\text{Hz}$ and $f_p = 1/12.1\,\text{Hz}$ correspond to the typical peak frequency range for sea-state conditions. For these cases, the solutions obtained from GNL-FEM and MoorDyn demonstrate strong agreement, with the maximum discrepancy being less than 2.5%. Both models effectively capture the dynamic and nonlinear characteristics of the system.

The excitation frequency $f_p = 1/20.0\,\text{Hz}$ corresponds to the scenario of swell waves, which can induce significant surge motion in a floating structure. The comparison between GNL-FEM and MoorDyn results for this case shows good agreement. However, during the return cycle, the line becomes slack, and upon regaining tension, the MoorDyn simulation exhibits pronounced oscillations in the time series, which are not observed in the GNL-FEM results.

To further examine the slacking behaviour of the line in this scenario, we visualise the line shape at four different time instances in Fig. 19, along with the corresponding local principal stress distribution. Additionally, we present the tension along the line at 10 different time instances in Fig. 20a, and the simultaneous time-series plot of tension at the fairlead and anchor in Fig. 20b.

We focus on monitoring the 14th excitation cycle to analyse the dynamic behaviour of the line. Between $tf_p = 13.75$ and $tf_p = 14.25$, the fairlead moves to the right (+X), causing the line to undergo tensioning, as observed in Fig. 20b. Subsequently, from $tf_p = 14.25$ to $tf_p = 14.75$, the fairlead moves towards the left (−X), reaching peak velocity at $tf_p = 14.5$. Due to this rapid return motion, a transverse wave propagates from the fairlead towards the anchor. As the transverse wave reaches the seabed, it interacts with the contact point, leading to localised peak stresses, as evident in Figs. 19c, d, and 20a at $tf_p \in \{14.5, 14.6, 14.7\}$. During this period, the anchor has zero tension. Once the fairlead starts moving rightward again, the line regains tension, thereby repeating the cycle. This example thus highlights the interplay between line dynamics and seabed interaction.

To examine the other extreme of the frequency spectrum, we consider an excitation frequency of $f_p = 1/0.2 = 5\,\text{Hz}$. While this is unusually high for wind-generated waves, it serves as a test case for scenarios where a floater may be excited by an eccentric rotating mass,

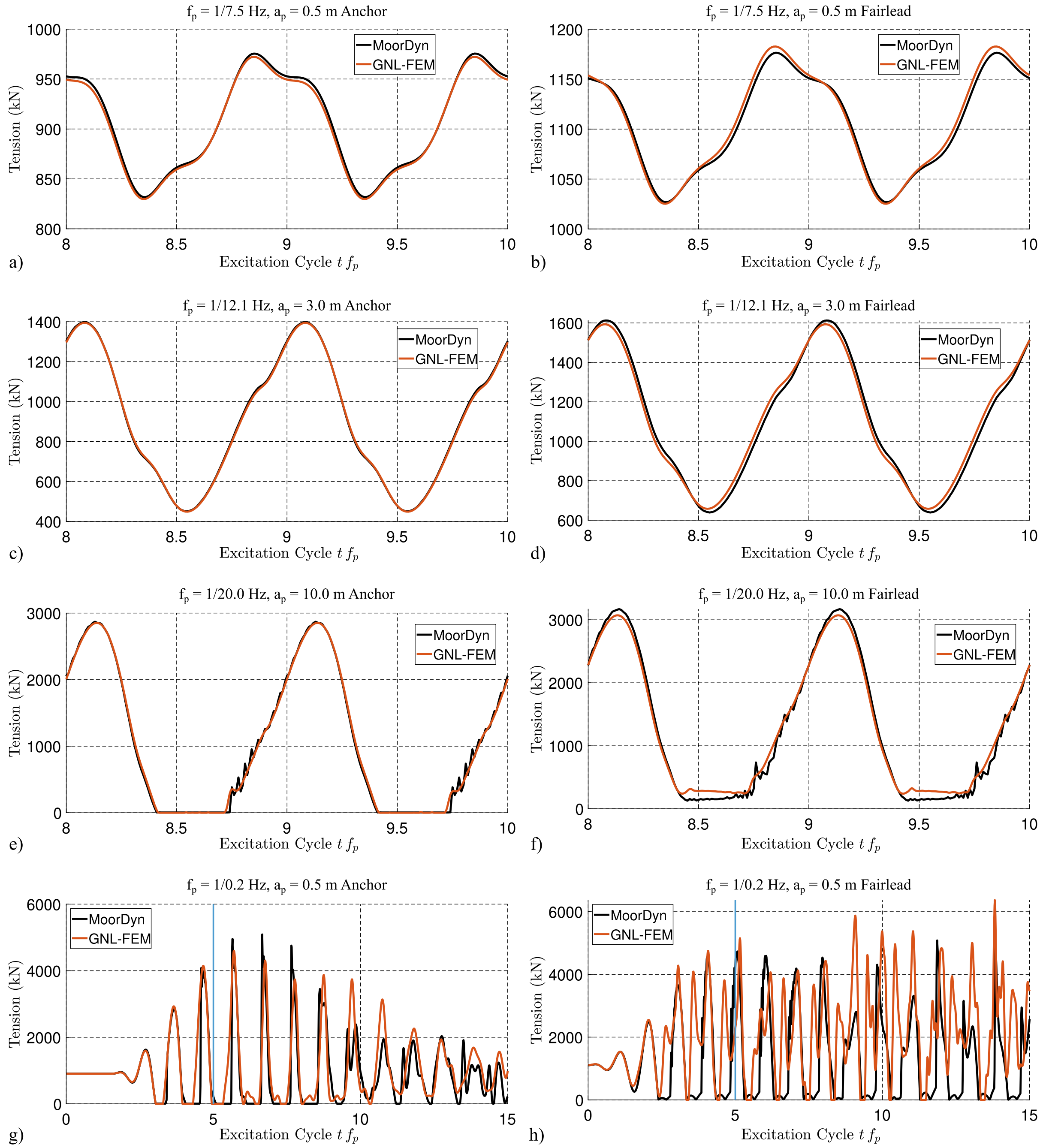


**Fig. 18.** Plots of tension at the fairlead and the anchor, comparing GNL-FEM and MoorDyn results for the catenary line Table 3, exposed to harmonic excitation at the fairlead. (a–b) $f_p = 1/7.50\,\text{Hz}$, $a_p = 0.5\,\text{m}$, (c–d) $f_p = 1/12.10\,\text{Hz}$, $a_p = 3.0\,\text{m}$, (e–f) $f_p = 1/20.0\,\text{Hz}$, $a_p = 10.0\,\text{m}$, (g–h) $f_p = 1/0.2\,\text{Hz}$, $a_p = 0.5\,\text{m}$.

**Table 4**
Comparison of the GNL-FEM and MoorDyn results at the anchor and the fairlead.

| Excitation frequency $f_p$ | Excitation amplitude $a_p$ | Difference at anchor $P_d$ Anchor | Difference at fairlead $P_d$ Fairlead |
|---|---|---|---|
| 1/7.5 Hz | 0.5 m | 0.0035 | 0.0043 |
| 1/12.1 Hz | 3.0 m | 0.0054 | 0.0247 |
| 1/20.0 Hz | 10.0 m | 0.0353 | 0.0589 |
| 1/0.2 Hz | 0.5 m | 0.4764 | 0.8731 |

such as an imbalanced wind turbine. Under these conditions, the line exhibits highly dynamic behaviour, preventing the system from reaching a steady state. The differences between GNL-FEM and MoorDyn are particularly pronounced at the fairlead, where the effects of dynamic excitation are strongest. However, as the line approaches the anchor, the combined effects of non-linearities and seabed interaction shift the energy towards lower frequencies. Consequently, the discrepancy between GNL-FEM and MoorDyn is less significant at the anchor.

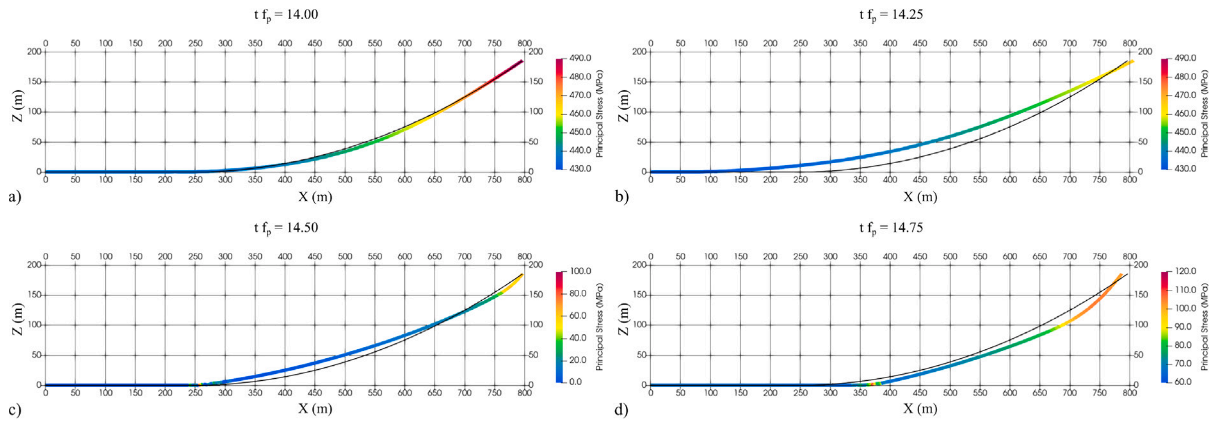


**Fig. 19.** Snapshots of the catenary mooring line at four instances in a excitation cycle for $f_p = 1/20\,\mathrm{Hz}$, $a_p = 10.0\,\mathrm{m}$. The colour of the line represents local principal stress.

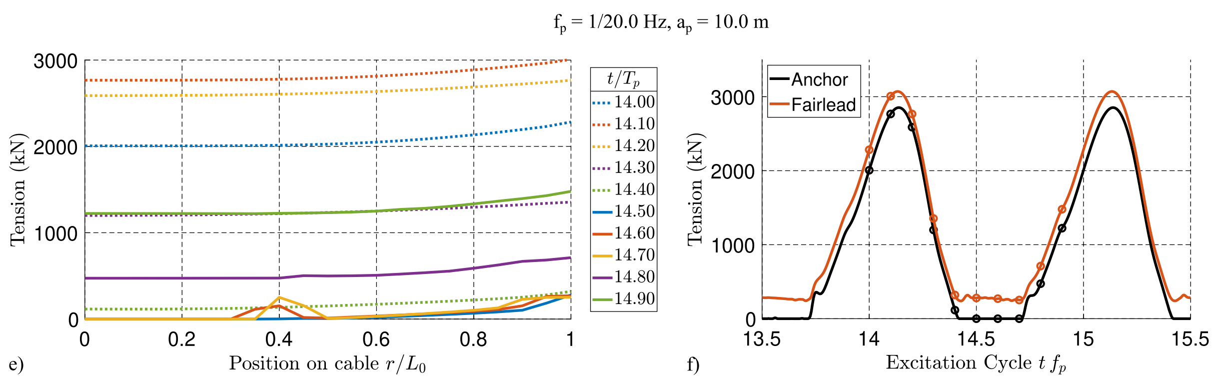


**Fig. 20.** (a) Plots showing the tension distribution along the line at 10 different time instances within an excitation cycle for the case $f_p = 1/20.0\,\mathrm{Hz}$, $a_p = 10\,\mathrm{m}$. (b) Time-series plots of the tension at the fairlead and anchor, with markers indicating the specific time instances at which the tension distribution along the line is plotted in Fig. 20a.

The differences observed between GNL-FEM and MoorDyn in the slack-taut and high-frequency excitation cases are due to two compounding factors. First, in the lumped mass approach the strain is computed as a constant value per segment, whereas in GNL-FEM the strain field is derived from the surface deformation gradient $\mathbf{F}_\Gamma$ and varies continuously along the line through the polynomial basis functions. This continuous strain representation allows GNL-FEM to capture the propagation of stress waves during sharp dynamic events, which the segment-level strain in MoorDyn cannot resolve resulting in spurious oscillations. Second, the explicit RK4 time-stepping scheme employed in MoorDyn lacks high-frequency numerical dissipation, unlike the Generalised-$\alpha$ scheme in GNL-FEM, which suppresses spurious high-frequency oscillations while preserving the low-frequency response.

## 5. Conclusions

This manuscript presents a formulation of the finite-strain, large-deformation mooring dynamics boundary value problem using the principles of Tangential Differential Calculus (TDC). The motivation for adopting the TDC framework lies in its natural suitability for curved manifolds and its versatility in numerical implementation, accommodating both embedded and parametric approaches. The manuscript presents a finite element-based solution procedure, referred to as GNL-FEM, to model the boundary value problem for general mooring dynamics scenarios, ranging from catenary to taut mooring lines. The implementation of GNL-FEM is described briefly, highlighting its development in the *Julia* programming language using the *Gridap.jl* finite element library, which enables an efficient and easily reproducible computational framework. Additionally, based on the same TDC-based formulation, the manuscript introduces a reduced-order analytical model, termed GNL-ANA, specifically designed for taut mooring systems.

The manuscript demonstrates the robustness of GNL-FEM, via a mesh ($h$), element order ($p$) and time-step $\Delta t$ refinement study, where the model is demonstrated to exhibit optimal convergence rate. GNL-FEM implementation is further verified through a study of the geometrically nonlinear problem of elongation of flexible parabolic line under the action of its own weight. The accuracy of the implementation is presented through displacement field and the resulting elastic potential energy.

A major focus of the manuscript is to investigate the geometric nonlinearity in the dynamic response of taut mooring lines. The line is pre-tensioned to a specified level and subjected to dynamic excitation through periodic motion of the fairlead. The GNL-FEM model is employed to analyse this system, revealing that second-order nonlinearities dominate the response, as indicated by the presence of super-harmonics and sub-harmonics in the displacement field. Additionally, third-order non-linear effects are also observed. The strain field, derived from the displacement, exhibits localised peaks at the natural frequencies of the line. By analysing the response spectrum, the study captures how the influence of various natural frequencies evolves with changes in excitation frequency. The manucript reports a broad parametric study, covering a range of excitation frequencies, amplitudes, and pre-tension values for the taut line. The results demonstrate progressive hardening of the line, reflected by a rightward shift in the peaks of the strain response, with increasing excitation frequency and amplitude. This behaviour is also due to the geometric nonlinearity in the response.

The manuscript next investigates the range of applicability for the reduced order analytical model GNL-ANA, devised specifically for the taut mooring line. The analytical model is formulated using different number of sinusoidal shape functions defined along the line, with increasing accuracy when increasing the number of shape functions. With the use of five shape functions, the reduced order model is demonstrated to show acceptable accuracy up-to the second natural frequency of the system, even for the high excitation amplitude and high pre-tensioning scenarios. This highlights that potential of such reduced order models, thus encouraging their use for low-fidelity analysis such as material optimisation or understanding temperature concentration.

Finally, GNL-FEM is applied to catenary line problem, including the sea-bed interaction and self drag. The analysis is done for a chain line, with low frequency excitation corresponding to swell waves response of a floater, and high frequency excitation corresponding to wind-waves response of a floater. For all of these cases, GNL-FEM is shown to have good comparison against the established lumped mass model Moordyn (Hall and Goupee, 2015), including for the cases where the line become slack. Finally, both GNL-FEM and Moordyn are used to simulate a hypothetical scenario involving very high-frequency excitation, which could arise from events such as eccentric rotation of a wind turbine due to damage or extreme operating conditions. In this case, the responses predicted by GNL-FEM and Moordyn differ, highlighting the need for further investigation into the effects of high-frequency excitation at the fairlead, beyond the typical frequencies associated with ocean waves.

The continuous definition of differential and geometric quantities in TDC also allows easy implementation of dynamic non-linear material stiffness. In our work (Agarwal and Colomés, 2025), we have extended GNL-FEM to incorporate the non-linear and dynamic Schapery viscoelastic material model for synthetic mooring lines. The key challenge in this extension is that the Schapery model is compliance-based, while GNL-FEM framework is displacement-based. This is addressed in Agarwal and Colomés (2025) using a predictor–corrector incremental strain approach, with the hereditary integral tracked at each quadrature point. Moreover, owing to the robustness of GNL-FEM, in our work (Santjer et al., 2025), we have utilised GNL-FEM for studying the mooring dynamics for a catenary line in 11 different locations in the Dutch North Sea. For each location, the line was exposed to local ocean current and irregular wave excitation from 300 different sea-states, where for each sea-state the line response for simulated for a standard storm duration of 20 min. This data was used for building a Bayesian network, determining the influence of hydrodynamic variables on tension rates on these mooring lines. This manuscript was focused on setting up the boundary value problem and defining the solution procedure.

In our future work, our focus is to expand this approach to mooring lines in 3D domain. This current 2D implementation has can be readily expanded to 3D by defining a pair of normals orthogonal to the computed tangent from Section 2.1. Furthermore, the effects of torsional stiffness and bending for the cables and chains with higher bending stiffness will be implemented by computing the curvature based on the Weingarten map (Kaiser and Fries, 2023). Through this step-by-step approach, our aim is to extend the framework to multi-segment, multi-line systems, subjected to multi-directional loading, thereby demonstrating its broader potential.

## CRediT authorship contribution statement

**Shagun Agarwal:** Writing – original draft, Visualization, Software, Methodology, Investigation, Formal analysis, Conceptualization. **Sergio Sánchez Gómez:** Writing – review & editing, Software, Methodology, Investigation, Conceptualization. **Oriol Colomés:** Writing – review & editing, Software, Methodology, Funding acquisition, Conceptualization.

## Declaration of competing interest

The authors declare that they have no known competing financial interests or personal relationships that could have appeared to influence the work reported in this paper.

## Acknowledgements

The authors acknowledge the use of *Snellius*, the national supercomputer hosted by *SURF* under the project *EINF-7558*; and the Delft-Blue supercomputer, hosted by Delft High Performance Computing Centre (https://www.tudelft.nl/dhpc), for providing the computational resources required for this work. This publication is part of the project MERGANSER with file number DEI122010 of the programme DEI+ from the Netherlands Enterprise Agency (RVO).

## Appendix. Derivation of the equation of motion for a low order 1D continuum based on the lagrangian formalism

In this section the Lagrangian form of equations of motion of a one dimensional system whose motion is defined in the region $s = \{a \leq x \leq b\}$ are derived by means of the Hamilton-Ostrogradsky principle. Employing this principle, it must take into account that the Lagrangian density $\lambda$ is a function that may depend on higher order spatial derivatives. Given that, the Lagrangian density function employing index notation is defined as:

$$\lambda = \lambda\left(t, x, u_i, \dot{u}_i, u_{i,j}\right) \tag{56}$$

The external energy density $w_{\text{ext}}$ and the dissipation energy density $\mathscr{D}_{\text{diss}}$ describe the energy generated by generalised external distributed forces (concentrated forces can also be considered making use of the Dirac delta function) and the dissipative energy, respectively.

$$\mathscr{V}_{\text{ext}} = \mathscr{V}_{\text{ext}}\left(t, x, u_i\right) \tag{57}$$

$$\mathscr{D}_{\text{diss}} = \mathscr{D}_{\text{diss}}\left(t, x, \dot{u}_i\right) \tag{58}$$

where, $u_i$ is the generalised coordinate, the $(,)$ denotes the spacial derivative, and the $\dot{()}$ denotes the time derivative. To obtain the Lagrangian form of the equation of motion and boundary conditions, the variational principle is employed. To this end, let us first consider a perturbed displacement $X_i$ of the real displacement $u_i$ in the following form:

$$X_i(x,t) = u_i(x,t) + \varepsilon\xi_i(x,t) \tag{59}$$

where $\varepsilon$ is the quantity of the perturbation, $\xi_i$ is a normalised perturbation. Let us suppose that these two arbitrary displacements $X_i$ and $u_i$ describe the motions of the continuum during the time interval $\alpha < t < \beta$, and that the perturbations at the time extremes $\alpha$ and $\beta$ are zero, such that:

$$\xi_i(x,\alpha) = \xi_i(x,\beta) = 0 \tag{60}$$

The Hamilton-Ostrogradsky principle states that,

$$\frac{d}{d\varepsilon}\left[\int_\alpha^\beta \int_s \lambda \; ds dt\right]_{\varepsilon=0} = 0 \tag{61}$$

and leads to,

$$\int_\alpha^\beta \left[\int_s \left(\frac{\partial\lambda}{\partial u_i}\xi_i + \frac{\partial\lambda}{\partial\dot{u}_i}\dot{\xi}_i + \frac{\partial\lambda}{\partial u_{i,j}}\xi_{i,j}\right) ds\right] dt = 0 \tag{62}$$

elaborating the terms, the following relations, that ensure uniqueness in Eq. (62) are used.

$$\begin{aligned} \frac{\partial\lambda}{\partial\dot{u}_i}\dot{\xi}_i &= \frac{\partial}{\partial t}\left(\xi_i\frac{\partial\lambda}{\partial\dot{u}_i}\right) - \xi_i\frac{\partial}{\partial t}\frac{\partial\lambda}{\partial\dot{u}_i} \\ \frac{\partial\lambda}{\partial u_{i,j}}\xi_{i,j} &= \frac{\partial}{\partial x_j}\left(\xi_i\frac{\partial\lambda}{\partial u_{i,j}}\right) - \xi_i\frac{\partial}{\partial x_j}\frac{\partial\lambda}{\partial u_{i,j}} \end{aligned} \tag{63}$$

Substituting the terms in Eq. (63) into Eq. (62), and applying Gauss divergence theorem the following expression is obtained:

$$\int_{\alpha}^{\beta}\left\{\int_{s}\xi_i\left(\frac{\partial\lambda}{\partial u_i}+\frac{\partial}{\partial t}\frac{\partial\lambda}{\partial\dot{u}_i}+\frac{\partial}{\partial x_j}\frac{\partial\lambda}{\partial u_{i,j}}\right)ds-\xi_i\frac{\partial\lambda}{\partial u_{i,j}}\bigg|_{s=a}^{s=b}\right\}dt \\ -\int_{s}\xi_i\frac{\partial\lambda}{\partial\dot{u}_i}\bigg|_{\alpha}^{\beta}ds=0. \tag{64}$$

Setting to zero the integrand of the first integral in Eq. (64), and introducing the dissipative function (Eq. (58)), we obtain the equation of motion in the Lagrangian form:

$$\frac{\partial\lambda}{\partial u_i}+\frac{\partial}{\partial t}\frac{\partial\lambda}{\partial\dot{u}_i}+\frac{\partial}{\partial x_j}\frac{\partial\lambda}{\partial u_{i,j}}+\frac{\partial\mathscr{D}_{\mathrm{diss}}}{\partial\dot{u}_i}=0 \tag{65}$$

with the following natural boundary condition

$$-\frac{\partial\lambda}{\partial u_{i,j}}\bigg|_{s=a}^{s=b}=\overline{T} \tag{66}$$

## References


Agarwal, S., Colomés, O., 2025. Finite-element model for geometric nonlinearity and dynamic stiffness of synthetic mooring lines. In: Proceedings of 35th International Ocean and Polar Engineering Conference. Seoul, South Korea.

Aliyar, S., Ducrozet, G., Bouscasse, B., Bonnefoy, F., Sriram, V., Ferrant, P., 2022. Numerical coupling strategy using HOS-OpenFOAM-MoorDyn for OC3 Hywind SPAR type platform. Ocean Eng. 263, 112206. http://dx.doi.org/10.1016/j.oceaneng.2022.112206.

Bach-Gansmo, M.T., Garvik, S.K., Thomsen, J.B., Andersen, M.T., 2020. Parametric study of a taut compliant mooring system for a FOWT compared to a catenary mooring. J. Mar. Sci. Eng. 8 (6), 431. http://dx.doi.org/10.3390/jmse8060431.

Badia, S., Verdugo, F., 2020. Gridap: An extensible Finite Element toolbox in Julia. J. Open Source Softw. 5 (52), 2520. http://dx.doi.org/10.21105/joss.02520.

Banks, H.T., Hu, S., Kenz, Z.R., 2011. A brief review of elasticity and viscoelasticity for solids. Adv. Appl. Math. Mech. 3 (1), 1–51. http://dx.doi.org/10.4208/aamm.10-m1030.

Bhuiyan, M.A., Hu, P., Khare, V., Hamaguchi, Y., Thakur, B.K., Rahman, M.K., 2022. Economic feasibility of marine renewable energy. Front. Mar. Sci. 9, 988513. http://dx.doi.org/10.3389/fmars.2022.988513.

Bilgili, M., Alphan, H., 2022. Global growth in offshore wind turbine technology. Clean Technol. Environ. Policy 24 (7), 2215–2227. http://dx.doi.org/10.1007/s10098-022-02314-0.

Bivol, I., Jeffcoate, P., Johanning, L., Nicoll, R., 2017. PLAT-O# 2 at FloWave: A tank-scale validation of ProteusDS dynamic analysis tool for floating tidal. In: Proc. EWTEC'17.

Buckham, B., Driscoll, F.R., Nahon, M., 2004. Development of a finite element cable model for use in low-tension dynamics simulation. J. Appl. Mech. 71 (4), 476–485. http://dx.doi.org/10.1115/1.1755691.

Campanile, A., Piscopo, V., Scamardella, A., 2018. Mooring design and selection for floating offshore wind turbines on intermediate and deep water depths. Ocean Eng. 148, 349–360. http://dx.doi.org/10.1016/j.oceaneng.2017.11.043.

Cao, Q., Goswami, S., Tripura, T., Chakraborty, S., Karniadakis, G.E., 2024. Deep neural operators can predict the real-time response of floating offshore structures under irregular waves. Comput. Struct. 291, 107228.

Castro-Santos, L., Filgueira-Vizoso, A., Carral-Couce, L., Formoso, J.Á.F., 2016. Economic feasibility of floating offshore wind farms. Energy 112, 868–882. http://dx.doi.org/10.1016/j.energy.2016.06.135.

Chatjigeorgiou, I.K., Mavrakos, S.A., 2016. Cable dynamics for marine applications. In: Springer Handbook of Ocean Engineering. Springer, pp. 875–906. http://dx.doi.org/10.1007/978-3-319-16649-0_38.

Chen, L., Basu, B., Nielsen, S.R., 2018. A coupled finite difference mooring dynamics model for floating offshore wind turbine analysis. Ocean Eng. 162, 304–315.

Chen, M., Li, C.B., Han, Z., Lee, J.-b., 2023. A simulation technique for monitoring the real-time stress responses of various mooring configurations for offshore floating wind turbines. Ocean Eng. 278, 114366. http://dx.doi.org/10.1016/j.oceaneng.2023.114366.

Chung, J., Hulbert, G.M., 1993. A time integration algorithm for structural dynamics with improved numerical dissipation: The generalized-alpha method. J. Appl. Mech. 60 (2), 371–375. http://dx.doi.org/10.1115/1.2900803.

Crespo, A., Gómez-Gesteira, M., Dalrymple, R., 2007. 3D SPH Simulation of large waves mitigation with a dike. J. Hydraul. Res. 45 (5), 631–642. http://dx.doi.org/10.1080/00221686.2007.9521799.

Delfour, M., Zolésio, J., 1996. Tangential differential equations for dynamical thin/shallow shells. J. Differential Equations 128 (1), 125–167. http://dx.doi.org/10.1006/jdeq.1996.0092.

Depalo, F., Wang, S., Xu, S., Guedes Soares, C., Yang, S.-H., Ringsberg, J.W., 2022. Effects of dynamic axial stiffness of elastic moorings for a wave energy converter. Ocean Eng. 251, 111132. http://dx.doi.org/10.1016/j.oceaneng.2022.111132.

Domínguez, J.M., Crespo, A.J., Hall, M., Altomare, C., Wu, M., Stratigaki, V., Troch, P., Cappietti, L., Gómez-Gesteira, M., 2019. SPH simulation of floating structures with moorings. Coast. Eng. 153, 103560. http://dx.doi.org/10.1016/j.coastaleng.2019.103560.

Escalante, M.R., Sampaio, R.R., Rosales, M.B., Ritto, T., 2011. A reduced order model of a 3D cable using proper orthogonal decomposition. Mec. Comput. 30 (13), 1143–1158.

Fries, T., Schöllhammer, D., 2020. A unified finite strain theory for membranes and ropes. Comput. Methods Appl. Mech. Engrg. 365, 113031. http://dx.doi.org/10.1016/j.cma.2020.113031.

Gobat, J., Grosenbaugh, M., 2001. Application of the generalized-alpha method to the time integration of the cable dynamics equations. Comput. Methods Appl. Mech. Engrg. 190 (37–38), 4817–4829. http://dx.doi.org/10.1016/S0045-7825(00)00349-2.

Guo, B., Ringwood, J.V., 2021. A review of wave energy technology from a research and commercial perspective. IET Renew. Power Gener. 15 (14), 3065–3090. http://dx.doi.org/10.1049/rpg2.12302.

Haj-Ali, R.M., Muliana, A.H., 2004. Numerical finite element formulation of the Schapery non-linear viscoelastic material model. Internat. J. Numer. Methods Engrg. 59 (1), 25–45. http://dx.doi.org/10.1002/nme.861.

Hall, M., 2020. MoorDyn V2: New capabilities in mooring system components and load cases. In: Volume 9: Ocean Renewable Energy. American Society of Mechanical Engineers, Virtual, Online, V009T09A078. http://dx.doi.org/10.1115/OMAE2020-19341.

Hall, M., Goupee, A., 2015. Validation of a lumped-mass mooring line model with DeepCwind semisubmersible model test data. Ocean Eng. 104, 590–603. http://dx.doi.org/10.1016/j.oceaneng.2015.05.035.

Harnois, V., Thies, P.R., Johanning, L., 2016. On peak mooring loads and the influence of environmental conditions for marine energy converters. J. Mar. Sci. Eng. 4 (2), 29. http://dx.doi.org/10.3390/jmse4020029.

Harris, R.E., Johanning, L., Wolfram, J., 2004. Mooring systems for wave energy converters: A review of design issues and choices. pp. 180–189, Marec2004.

Hennessey, C., Pearson, N., Plaut, R.H., 2005. Experimental snap loading of synthetic ropes. Shock Vib. 12 (3), 163–175. http://dx.doi.org/10.1155/2005/734345.

Inc, A., 2024. Aqwa theory manual. URL https://ansyshelp.ansys.com/public//Views/Secured/corp/v242/en/aqwa_thy/aqwa_thy.html.

Jeffcoate, P., Fiore, F., O'Farrell, E., Starzmann, R., Bischof, S., 2016. Comparison of simulations of taut-moored platform PLAT-O using ProteusDS with experiments. In: Proceedings of AWTEC.

Kaiser, M.W., Fries, T.-P., 2023. Curved, linear Kirchhoff beams formulated using tangential differential calculus and Lagrange multipliers. Proc. Appl. Math. Mech. 22 (1), e202200042. http://dx.doi.org/10.1002/pamm.202200042.

Kanotra, R., Shankar, R., 2022. Floating solar photovoltaic mooring system design and analysis. In: OCEANS 2022-Chennai. IEEE, pp. 1–9. http://dx.doi.org/10.1109/OCEANSChennai45887.2022.9775352.

Li, C.B., Choung, J., 2021. Effects of strain- and strain rate- dependent nonlinear mooring line stiffness on floating platform motion. Ocean Eng. 241, 110011. http://dx.doi.org/10.1016/j.oceaneng.2021.110011.

Li, M., Luo, H., Zhou, S., Kumar, G.M.S., Guo, X., Law, T.C., Cao, S., 2022. State-of-the-art review of the flexibility and feasibility of emerging offshore and coastal ocean energy technologies in East and Southeast Asia. Renew. Sustain. Energy Rev. 162, 112404. http://dx.doi.org/10.1016/j.rser.2022.112404.

Lozon, E., Hall, M., 2023. Coupled loads analysis of a novel shared-mooring floating wind farm. Appl. Energy 332, 120513. http://dx.doi.org/10.1016/j.apenergy.2022.120513.

Macdonald, J., 2016. Multi-modal vibration amplitudes of taut inclined cables due to direct and/or parametric excitation. J. Sound Vib. 363, 473–494. http://dx.doi.org/10.1016/j.jsv.2015.11.012, URL https://linkinghub.elsevier.com/retrieve/pii/S0022460X15009098.

Mahfouz, M.Y., Lozon, E., Hall, M., Cheng, P.W., 2024. Integrated floating wind farm layout design and mooring system optimization to increase annual energy production. In: Journal of Physics: Conference Series. Vol. 2767, IOP Publishing, 062020. http://dx.doi.org/10.1088/1742-6596/2767/6/062020.

Maienza, C., Avossa, A.M., Picozzi, V., Ricciardelli, F., 2022. Feasibility analysis for floating offshore wind energy. Int. J. Life Cycle Assess. 27 (6), 796–812. http://dx.doi.org/10.1007/s11367-022-02055-8.

Masciola, M., Jonkman, J., Robertson, A., 2014. Extending the capabilities of the mooring analysis program: A survey of dynamic mooring line theories for integration into FAST. In: Volume 9A: Ocean Renewable Energy. American Society of Mechanical Engineers, San Francisco, California, USA, V09AT09A032. http://dx.doi.org/10.1115/OMAE2014-23508.

Mavrakos, S., Papazoglou, V., Triantafyllou, M., Hatjigeorgiou, J., 1996. Deep water mooring dynamics. Mar. Struct. 9 (2), 181–209. http://dx.doi.org/10.1016/0951-8339(94)00019-O.

Nayfeh, A.H., Mook, D.T., 1995. Nonlinear Oscillations.

Nguyen, N., Thiagarajan, K., 2022. Nonlinear viscoelastic modeling of synthetic mooring lines. Mar. Struct. 85, 103257. http://dx.doi.org/10.1016/j.marstruc.2022.103257.

Niosi, F., Begovic, E., Bertorello, C., Rinauro, B., Sannino, G., Bonfanti, M., Sirigu, S., 2023. Experimental validation of Orcaflex-based numerical models for the PEWEC device. Ocean Eng. 281, 114963. http://dx.doi.org/10.1016/j.oceaneng.2023.114963.

Niosi, F., Dell'edera, O., Glorioso, M., Paduano, B., Giorgi, G., Schreier, S., 2025. Experimental investigation and dataset release of a taut-leg mooring system for a semi-submersible floating offshore wind turbine. Ocean Eng. 328, 121067. http://dx.doi.org/10.1016/j.oceaneng.2025.121067.

Ocean, D., 2018. ProteusDS manual.

Orcina, A., 2014. OrcaFlex manual.

Palm, J., Eskilsson, C., Bergdahl, L., 2017. An hp -adaptive discontinuous Galerkin method for modelling snap loads in mooring cables. Ocean Eng. 144, 266–276. http://dx.doi.org/10.1016/j.oceaneng.2017.08.041.

Pham, T.-D., Dinh, M.-C., Kim, H.-M., Nguyen, T.-T., 2021. Simplified floating wind turbine for real-time simulation of large-scale floating offshore wind farms. Energies 14 (15), 4571. http://dx.doi.org/10.3390/en14154571.

Qiao, D., Li, P., Ma, G., Qi, X., Yan, J., Ning, D., Li, B., 2021. Realtime prediction of dynamic mooring lines responses with LSTM neural network model. Ocean Eng. 219, 108368. http://dx.doi.org/10.1016/j.oceaneng.2020.108368.

Qiao, D., Yan, J., Liang, H., Ning, D., Li, B., Ou, J., 2020. Analysis on snap load characteristics of mooring line in slack-taut process. Ocean Eng. 196, 106807. http://dx.doi.org/10.1016/j.oceaneng.2019.106807.

Qin, H., Peng, L., Wang, Z., Wu, S., He, W., Yang, Y., Li, J., Zhang, H., 2025. Wave motion response analysis of flip-type ocean aquaculture platforms based on AQWA. J. Mar. Sci. Eng. 13 (2), 211. http://dx.doi.org/10.3390/jmse13020211.

Roccia, B.A., Nguyen, T.-H., Veseth, P., Nielsen, F.G., Gebhardt, C.G., 2025. On the use of an advanced Kirchhoff rod model to study mooring lines. Mar. Struct. 104, 103883. http://dx.doi.org/10.1016/j.marstruc.2025.103883.

Santjer, R., Agarwal, S., Colomés, O., Morales-Napoles, O., 2025. Gaussian copula-based Bayesian networks for dynamic loads in mooring systems. http://dx.doi.org/10.2139/ssrn.5131622.

Sky, A., Hale, J.S., Zilian, A., Bordas, S.P., Neff, P., 2024. Intrinsic mixed-dimensional beam-shell-solid couplings in linear Cosserat continua via tangential differential calculus. Comput. Methods Appl. Mech. Engrg. 432, 117384. http://dx.doi.org/10.1016/j.cma.2024.117384.

Soares-Ramos, E.P., de Oliveira-Assis, L., Sarrias-Mena, R., Fernández-Ramírez, L.M., 2020. Current status and future trends of offshore wind power in Europe. Energy 202, 117787. http://dx.doi.org/10.1016/j.energy.2020.117787.

Vassalos, D., Kourouklis, A., 1998. An experimental, theoretical and full-scale investigation on the snap loading of marine cables. Main report.

Vilsen, S.A., Sauder, T., Sørensen, A.J., Føre, M., 2019. Method for real-time hybrid model testing of ocean structures: Case study on horizontal mooring systems. Ocean Eng. 172, 46–58.

Walton, T.S., Polachek, H., 1959. Calculation of nonlinear transient motion of cables.

Weller, S., Johanning, L., Davies, P., Banfield, S., 2015. Synthetic mooring ropes for marine renewable energy applications. Renew. Energy 83, 1268–1278. http://dx.doi.org/10.1016/j.renene.2015.03.058.

Wendt, F.F., Andersen, M.T., Robertson, A.N., Jonkman, J.M., 2016. Verification and validation of the new dynamic mooring modules available in FAST v8. In: Proceedings of the Twenty-Sixth (2016) International Ocean and Polar Engineering Conference. In: International Ocean and Polar Engineering Conference, Rhodes, Greece, URL https://onepetro.org/ISOPEIOPEC/proceedings/ISOPE16/All-ISOPE16/ISOPE-I-16-315/17681.

Xie, L., Li, C., Yue, M., He, H., Jia, W., Liu, Q., Xu, Z., Fan, L., Bashir, M., Yan, Y., 2024. Dynamic analysis of an improved shared moorings for floating offshore wind farm. Renew. Energy 232, 120963. http://dx.doi.org/10.1016/j.renene.2024.120963.

Xu, K., Larsen, K., Shao, Y., Zhang, M., Gao, Z., Moan, T., 2021. Design and comparative analysis of alternative mooring systems for floating wind turbines in shallow water with emphasis on ultimate limit state design. Ocean Eng. 219, 108377. http://dx.doi.org/10.1016/j.oceaneng.2020.108377.

Yu, Z., Ma, Q., Zheng, X., Liao, K., Sun, H., Khayyer, A., 2023. A hybrid numerical model for simulating aero-elastic-hydro-mooring-wake dynamic responses of floating offshore wind turbine. Ocean Eng. 268, 113050. http://dx.doi.org/10.1016/j.oceaneng.2022.113050.

Zhang, Y., Liu, H., 2023. Coupled dynamic analysis on floating wind farms with shared mooring under complex conditions. Ocean Eng. 267, 113323. http://dx.doi.org/10.1016/j.oceaneng.2022.113323.

Zhao, C., Stansby, P., Johanning, L., 2023. OrcaFlex predictions for a multi-float hinged WEC with nonlinear mooring systems: Elastic mooring force and dynamic motion. Ocean Eng. 286, 115504. http://dx.doi.org/10.1016/j.oceaneng.2023.115504.

Zhong, W., Zhao, W., Wan, D., Zhao, Y., 2024. Comparison study on mooring line models for hydrodynamic performances of floating offshore wind turbines. Ocean Eng. 296, 117083. http://dx.doi.org/10.1016/j.oceaneng.2024.117083.